

In situ measurement of the tensile strength of water

A. Andersen

Department of Physics and

Center for Fluid Dynamics

Technical University of Denmark

aand@fysik.dtu.dk

K. A. Mørch*

Department of Physics and

Center for Fluid Dynamics

Technical University of Denmark

morch@fysik.dtu.dk

ABSTRACT

We discuss a technique for in situ measurement of the tensile strength of water, i.e. the tensile strength inside a hydraulic system at the location where cavitation is expected to occur. A mechanically driven water-filled device, made from a transparent, open tube with a bottom the shape of a spherical cap, is used to generate a focused tensile stress wave in the water off the bottom. Bubbles produced in the bulk of water as well as at the stress-generating solid surface are recorded by high-speed digital video, and the tensile strength of the water is calculated from the initial growth rate of the individual bubbles. A qualitatively similar tube, but with a planar bottom, has been used earlier [1] for studying the collapse of one-dimensional cavity clusters, and some of the work presented in [1] is evaluated as a complement to the present study. Finally, the applicability of a medical, piezoelectric lithotripter for in situ measurement of the tensile strength of water is discussed.

NOMENCLATURE

D_h – measured horizontal bubble diameter
 D_v – measured vertical bubble diameter
 M – mass of primary device for acceleration (exclusive water)
 P_{imp} – momentum of the mass m at impact
 R – bubble radius
 TS – tensile strength of the liquid
 h_m – drop height of the mass m
 m – mass of impact body
 n_{H2O} – index of refraction for water
 p_v – vapour pressure
 p_∞ – local far field pressure around cavitation nucleus
 t – time
 ρ – density of the liquid

1. INTRODUCTION

Measurements of the tensile strength of water in hydrodynamic systems are usually performed by transfer of a sample of water to an external measuring device [2-3]. However, the tensile strength of technical water is not an invariant quantity,

and the transfer itself may change the tensile strength of the sample [4]. Therefore, tensile strength should be measured in situ using a focused tensile stress wave that generates cavitation off the solid boundaries of the hydraulic system considered.

In situ measurement of tensile strength of water was made in [5] with a medical piezoelectric lithotripter generating small clouds of cavitation bubbles in the bulk of water. In its normal mode of operation, the lithotripter produces a high-intensity compressive pressure pulse (typically up to 200-250 bar in the focal region) followed by a weaker tensile stress pulse. The latter produces cavitation if the tensile strength of the water is exceeded, and high-speed digital recordings of the initial bubble growth then allow calculation of the tensile strength. However, the value of tensile strength obtained is the tensile strength just *after* the water has been exposed to the compressive pressure pulse. In lithotripter experiments with Milli-Q water, seeded with spherical particles of highly corrugated surface, Arora, Ohl and Mørch [6] found that the particles caused cavitation not until the tensile stress in the lithotripter pulse exceeded 20 bar. Values of tensile strength that high are usually achieved only if special precautions are taken. Further, spherical particles with a very smooth surface, earlier tested in a venturi vortex flow to give a tensile strength below 1 bar [7], were unable to cause cavitation in the lithotripter experiments even at a tensile stress of 70 bar. Thus, it seems evident that the measurement of a true value of tensile strength in water requires the cavitation nuclei to experience *only* the tensile stress pulse that makes them explode into cavitation bubbles – a preceding compressive pulse expectedly increases the tensile strength.

At the WIMRC Cavitation Forum 2008 it was suggested by one of the present authors (KAM) [8] that the lithotripter pulse might be inverted to start with the tensile stress pulse, hereby allowing the true tensile strength of the liquid to be measured. At the meeting Professor Crum [9] pointed out that he had already tried to invert the pulse of his lithotripter, but had found that the erosive power of the lithotripter was completely lost. However, an explanation was not offered, and the tensile strength aspect was not discussed.

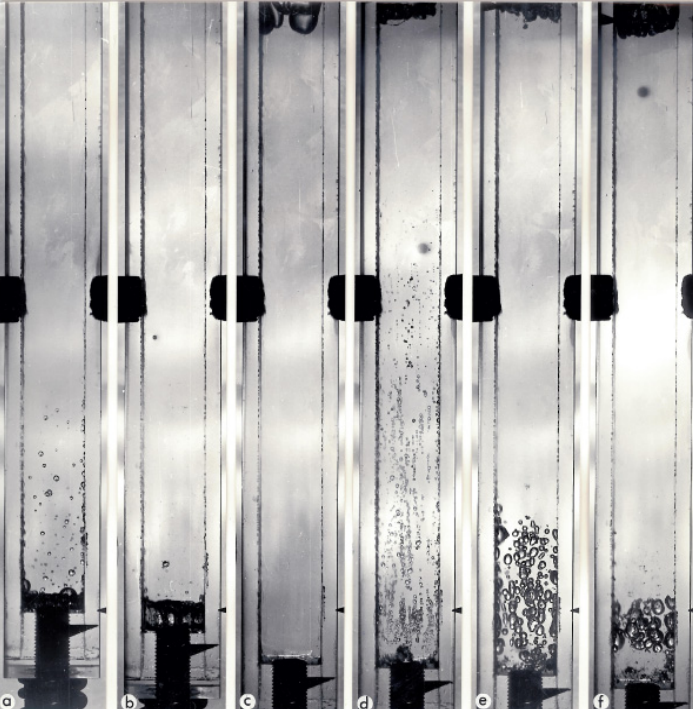


Figure 1. Cavitation generated in a water-filled tube (18 mm width \times 12 mm depth inside) with a planar bottom at strong, downward shock-acceleration of the tube [1]. Initially the bottom separates totally from the column of water above it, but when the separation-cavity collapses the resulting compression wave reflects at the free surface and produces an extended cavity cluster that subsequently collapses one-dimensionally. (a) $\Delta t = 1.3$ ms, (b) $\Delta t = 3.3$ ms, (c) $\Delta t = 7.8$ ms, (d) $\Delta t = 8.8$ ms, (e) $\Delta t = 10.8$ ms, and (f) $\Delta t = 12.8$ ms.

An understanding of what happens in a piezoelectric lithotripter, when driven with a high amplitude inverted pulse, may be obtained by experiments with a device qualitatively similar to the one used in [1], but modified to have a spherically shaped bottom. In [1] a vertical, water-filled rectangular tube with a planar bottom and a free upper water surface was used to generate and collapse one-dimensional cavity clusters in the column of water by knocking away the bottom from the column of water, initially at rest, Figure 1. The pressure recordings, made at the bottom, indicate a tensile strength at cavitation inception of at least 1 bar – a fairly high value, considering that no effort was made to achieve a high tensile strength in the water. We notice from Figure 1 that the planar walls, oriented in the direction of view, were seats of cavity nucleation in the subsequent cavitation processes within the column of water. The cavities observed in between these wall-nucleated cavities are estimated to have a similar number density, and therefore, most probably they were all nucleated on the front and back walls, not in the bulk of water where usually the tensile strength is higher than on the walls. This shows the need of modifying the equipment if it is to be used for tensile strength measurement. However, in [1] it was the wave and cavity cluster dynamics that were the subjects of study, not the tensile strength of the water.

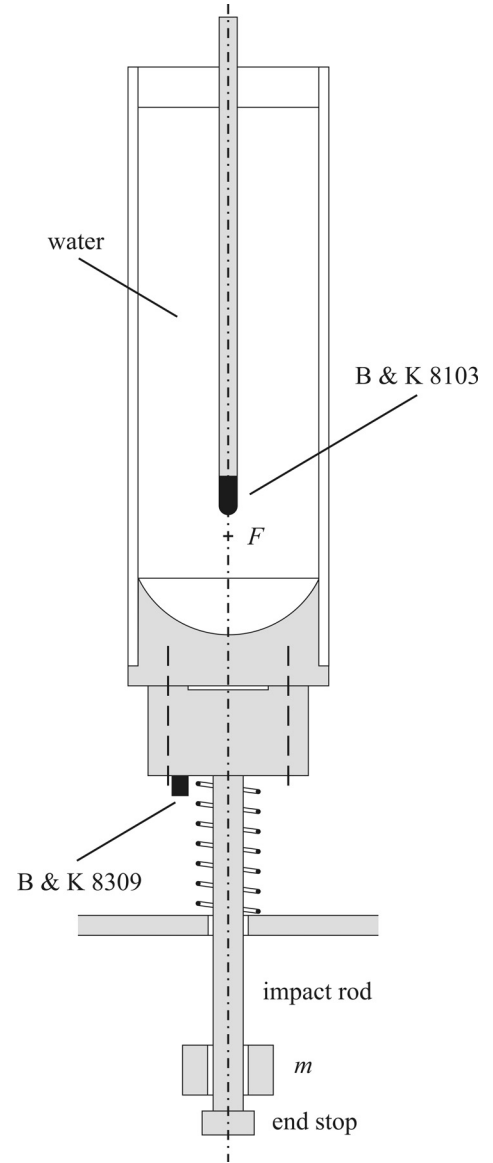


Figure 2. Experimental set up for in situ measurement of tensile strength of water. At the impact of the mass m onto the end stop of the impact rod a tensile stress wave, focused in the point F , is produced at the spherically shaped bottom of the tube, which is filled with water. The local motion of the device is recorded with a B&K 8309 accelerometer, and the stress wave above point F is recorded with a B&K 8103 hydrophone.

2. EXPERIMENTAL SET UP AND TECHNIQUE

We present experiments with focused tensile stress waves in water, produced by moderate downwards shock-acceleration of a vertical, cylindrical, transparent PMMA tube containing 1.5 liter of water with a free upper surface at atmospheric conditions, Figure 2. The tube has an inner diameter of 90 mm, and an aluminum bottom, the shape of a spherical cap with a radius of curvature of 50 mm. Its center F is on the axis of symmetry, 25 mm above the plane of the circumferential rim of the bottom. The water column has a height of 225 mm above this plane. The device, which has a mass $M = 2.1$ kg plus the mass of water, rests on a spring. The focused tensile stress wave in the water is

created by the impact of a brass weight of mass m , falling from a height h_m onto the end stop of an aluminum rod fixed to the lower bottom block, delivering its impact momentum P_{imp} to the device via a tensile stress pulse. The pulse is transferred to the upper bottom block through a contact zone of mean radius 30 mm. A longitudinal wave travels from here to the spherical solid-water interface where it arrives at annular segments, first at about the 30 mm radius, and subsequently at other radii, the delays depending on the distances the wave has to travel in the aluminum block, and on the transverse wave component travelling at lower velocity than the longitudinal component. Thus, the elements of the tensile stress wave in the liquid, generated at different annular segments of the spherical surface, though all focused on the same point F in the bulk of water, are not formed simultaneously. This limits the maximum of tensile stress that can be obtained at F , and increases the duration of the tensile stress pulse in the focal region. At the solid-water interface of the upper bottom block the strongest tensile stress is achieved where the wave first arrives, i.e. in the central region, while the wave intensity decreases towards the rim. However, the wave elements arriving in the focal zone from the different segments of the spherical surface build up a tensile stress higher than anywhere at the solid surface, and sufficient to reveal the tensile strength of the bulk water - but not without simultaneously generating cavitation at the solid-water interface of the bottom block where the tensile strength is smaller. No doubt, a piezoelectric focused wave generator, built to let a tensile stress wave lead the pulse, would be better suited for generating cavitation *only* in the focal region (if driven at a sufficient, but low amplitude), because in the piezoelectric device all the surface elements would be activated simultaneously and with equal strength.

The cavitation bubble dynamics is recorded by high-speed digital video using a Phantom v4.2 camera. From the observed initial growth of the individual cavitation bubbles, the tensile stress in the liquid at cavitation inception is calculated by use of the Rayleigh equation

$$R \frac{d^2 R}{dt^2} + \frac{3}{2} \left(\frac{dR}{dt} \right)^2 = -\frac{1}{\rho} (p_\infty - p_v) \quad (1)$$

where R is the bubble radius, ρ is the liquid density and p_∞ is the local far field pressure around the cavitation nucleus, while p_v is the vapour pressure. When a cavitation nucleus has grown beyond critical size, the cavitation bubble expands explosively, and at this time, chosen as time $t = 0$, the first term in Eq. (1) is negligible, and we find the tensile strength TS of the liquid from

$$TS = -(p_\infty - p_v)_{t=0} = \frac{3}{2} \rho \left[\left(\frac{dR}{dt} \right)^2 \right]_{t=0} \quad (2)$$

in which the initial bubble growth rate $(dR/dt)_{t=0}$ is obtained from the high-speed digital video.

A Brüel & Kjær type 8309 accelerometer is mounted beneath the lower aluminum block to record the motion of the system after impact of the mass m onto the end stop of the impact rod, and a Brüel & Kjær type 8103 hydrophone is used for recording the pressure pulse in the water a short distance above the focal region, Figure 2. The tensile strength cannot be measured with the hydrophone itself as its surface has its own

cavitation nuclei with their own critical size, probably giving a lower tensile strength than the nuclei in the bulk water.

The primary high-speed digital videos were taken horizontally, with the camera axis at the level of the focal point F . Cavitation bubbles generated below the plane of the rim of the spherically shaped bottom are therefore not visible. A consequence of the water-filled tube being of circular cross-section is that the bubbles are depicted horizontally distorted, depending on their position in the tube, while vertically their diameters are correctly depicted. Water has an index of refraction $n_{H_2O} = 1.333$ (that of PMMA is about 1.49, but with the tube wall being only 5 mm thick the difference is of minor importance). Bubbles formed on the axis of symmetry are elongated horizontally by a factor of n_{H_2O} . In the camera-device axis plane, bubbles formed on the frontal tube wall are not distorted, while at the rear tube wall they are horizontally elongated by the factor $2n_{H_2O}$. As a consequence, a bubble formed off-axis in lateral direction is also elongated horizontally, as on the axis, but in addition it appears further displaced laterally relative to its true position. The true bubble diameter is obtained from the observed vertical size, while the horizontal position of the bubble and its deformation tell where in the tube it is located.

3. EXPERIMENTS

Figure 3 shows an example of cavitation bubbles in water (distilled water from a tap in the university supply), generated by impact of a mass $m = 0.20$ kg from a height $h_m = 0.35$ m onto the end stop of the impact rod, and recorded horizontally at a framing rate of 8909 frames/s. We notice that cavitation bubbles first appear at the plane of the bottom rim, and then further up, and also, the bubbles are formed off-axis. In the first frame shown (time $t = 0$), bubbles have just developed to a visible size at the horizontal level of the focal point F , while near the plane of the rim of the bottom they are already in growth in the preceding frame (not shown).

Calculations of the critical pressure for 13 of the bubbles observed in the field of view give values of TS ranging from 0.15 bar to 0.61 bar, with a mean value $\langle TS \rangle = 0.35$ bar. Realizing that bubbles smaller than about 0.2 mm could not be observed, and that the expanded uncertainty of measurement (95% uncertainty level) of the bubble radii was about 0.1 mm it is clear that the tensile strength calculations have a significant uncertainty, estimated to be about 0.1 bar. This uncertainty is primarily due to the low framing rate and the limited resolution in the individual frames available with our equipment. No systematic pattern for the tensile strength distribution within the cluster can be identified.

The position of the cluster relative to the picture plane through the system axis is characterized by the mean of the ratios of measured horizontal to vertical bubble diameters D_H/D_V , and we find $\langle D_H/D_V \rangle = 1.45$. The standard uncertainty $u(D_H/D_V) = 0.14$ characterizes the spread of the bubble positions. Thus, the bubble cloud has its centre about 18 mm behind the picture plane through the axis. In Figure 3 the cluster centre appears to be displaced to the left by about 20 mm, but it is a consequence of the optical distortion. The real displacement is only about 14 mm. In Figure 4 data for bubble 5 of Figure 3 are shown.

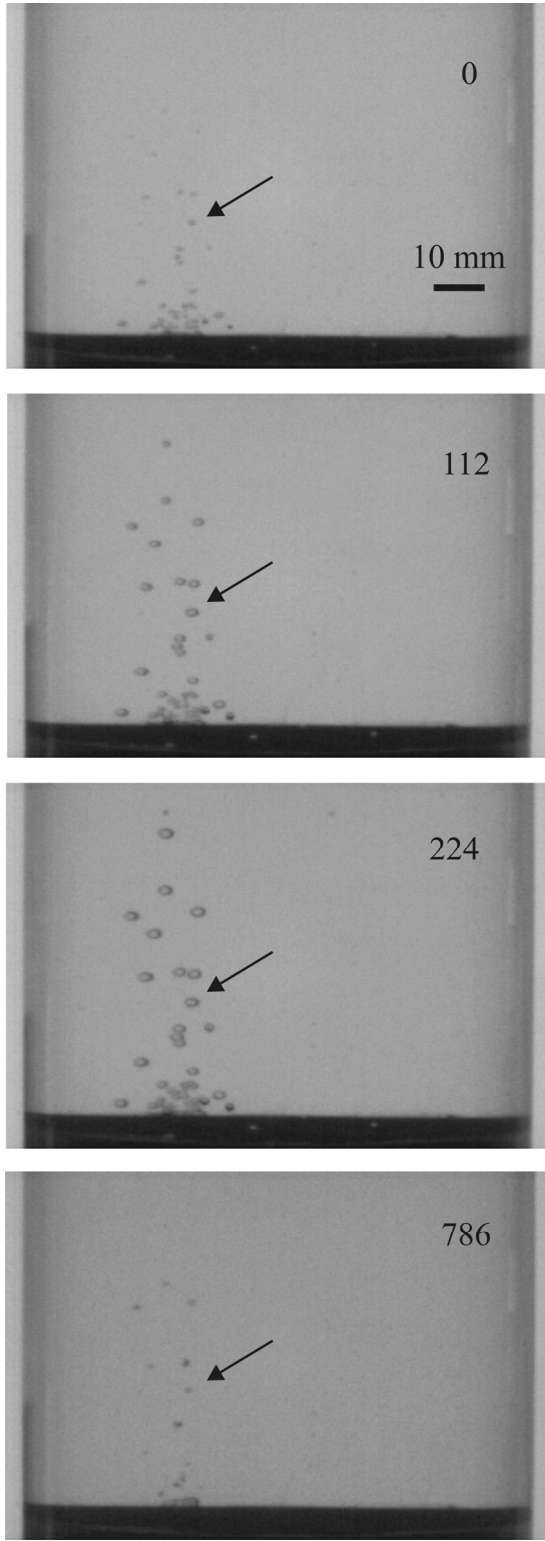


Figure 3. Cavitation at the impact of a mass of $m = 0.20$ kg from a height of $h_m = 0.35$ m (impact momentum $P_{imp} = 0.52$ kg m/s) onto the end stop of the impact rod. The time is indicated in μ s in each frame. The arrow points at bubble 5. The cavities develop first at the surface of the spherical bottom, and subsequently in the bulk of water above.

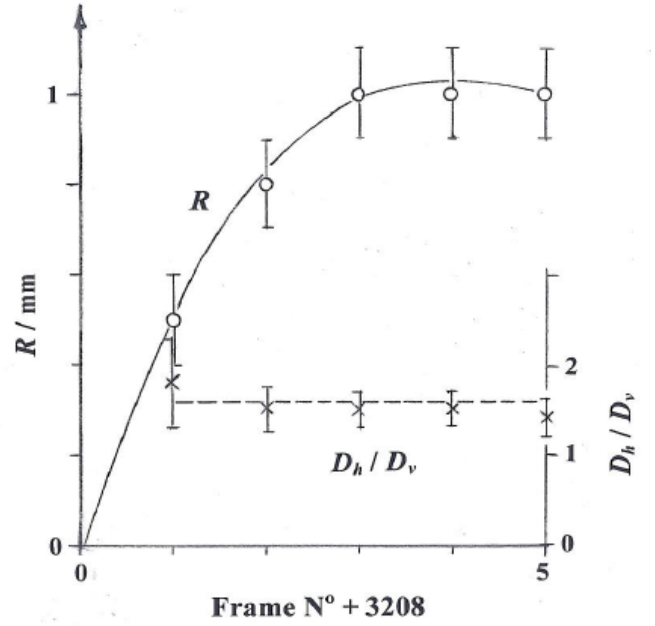


Figure 4. Bubble radii during the initial growth of bubble 5. Frame interval 112 μ s. For this bubble a value of $TS = 0.54$ bar is calculated, but we estimate $u(TS) = 0.1$ bar. The five frames used for determining the distortion of bubble 5 give $(D_h/D_v)_5 = 1.54$, $u(D_h/D_v)_5 = 0.07$. The error bars indicate expanded uncertainty.

The acceleration pulse producing a cavity cluster (as the one in Figure 3), and the associated pressure pulse, recorded above the focal point F , are shown in Figure 5. The impact of the mass m onto the end stop of the impact rod is partially elastic and the mass reaches a height of up to 10% of its initial drop height h_m after the impact. This allows us to calculate the motion of the centre of mass of the impacted system, but strong high-frequency standing waves (>10 kHz) in the system (filtered away from the recorded signals) and the complicated wave propagation make it difficult to set up reliable calculations of the local pressure causing cavity inception, but this is obtained experimentally from the observed bubble dynamics. We notice that the pressure pulse recorded with the hydrophone is delayed relative to the acceleration pulse by ~ 100 μ s due to the distance between the transducers. During the initial negative acceleration pulse the tensile stress increases in the water until critical conditions for the cavitation nuclei are exceeded; then pressure relaxation to the vapour pressure occurs. The tensile stress wave moves on to the surface of the water column where the atmospheric boundary causes wave reflection with a phase shift of π , and it moves back as a compressive wave. From Figure 5 the compression wave is seen to arrive at the hydrophone about 0.7 ms after relaxation of the tensile stress wave, indicating a wave velocity of about 600 m/s. This low velocity is ascribed to the elasticity of the PMMA tube.

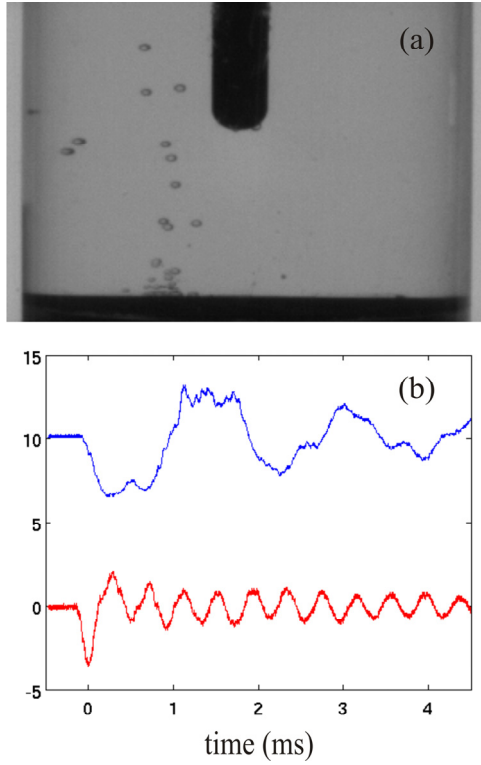


Figure 5. Cavitation experiment as in Figure 3, but with the hydrophone positioned at the axis of symmetry, 10 mm above the focal point F , its acoustic centre being a further 11 mm up. (a) High-speed digital recording of a cavitation event, the bubbles being at about their maximum size. $\langle TS \rangle = 0.38$ bar calculated from 8 bubbles covering the range of tensile stress $0.15 \text{ bar} \leq TS \leq 0.76 \text{ bar}$. (b) The pressure pulse (blue curve, 1 unit ~ 0.4 bar, starting at 1 bar) recorded at the acoustic centre of the hydrophone, and the acceleration pulse (red curve, 1 unit $\sim 0.5 \cdot 10^3 \text{ m/s}^2$) measured beneath the lower bottom block.

High-speed digital videos of cavitation bubbles, grown from nuclei on the spherical surface of the bottom, were obtained by observing the tube at an oblique angle of 22° with the horizontal plane, i.e. only the rear part of the bottom was visible. An example of a video taken at a framing rate of 4400 frames/s is shown in Figure 6. It is obtained with $P_{imp} = 0.48 \text{ kg m/s}$, i.e. slightly less than used for Figures 3, 4, and 5. Analysis was made for 10 of the bubbles, and the life cycles of the numbered ones are shown in Figure 7. The 5 bubbles forming a row in Figure 6 were reproducible in repeated experiments. They are located on the spherical bottom, bubble 1 about 15 mm behind the picture plane through the device axis, the other ones at increasing distances towards the rear. They are found to have a mean tensile strength of $\langle TS \rangle = 0.08$ bar, with $u(TS) = 0.02$ bar. In the last frame ($t = 681 \mu\text{s}$) bubble 1 and its immediate bottom-neighbours each leave a rebound cloud, indicating that they have just collapsed. Bubble 6 is one of two bubbles apparently located on the PMMA tube surface just above the upper bottom block, while bubble 8 is located on the edge of the spherical surface. Bubble 8 was found to develop also in a previous and in a subsequent experiment. The growth curves of the three surface-attached bubbles are essentially identical, and they are

delayed by about $50 \mu\text{s}$ relative to the first mentioned 5 bubbles on the bottom. Bubble 8 has a tensile strength of $TS = 0.13$ bar. Two bubbles, which are observed only in this experiment and show optical distortion, are bulk water bubbles. Thus, bubble 10 is estimated to be located 30 mm in front of the picture plane through the axis, and a $TS = 0.3$ bar is calculated, but with the bubble being visible only in 2 frames, this TS -calculation is very uncertain.

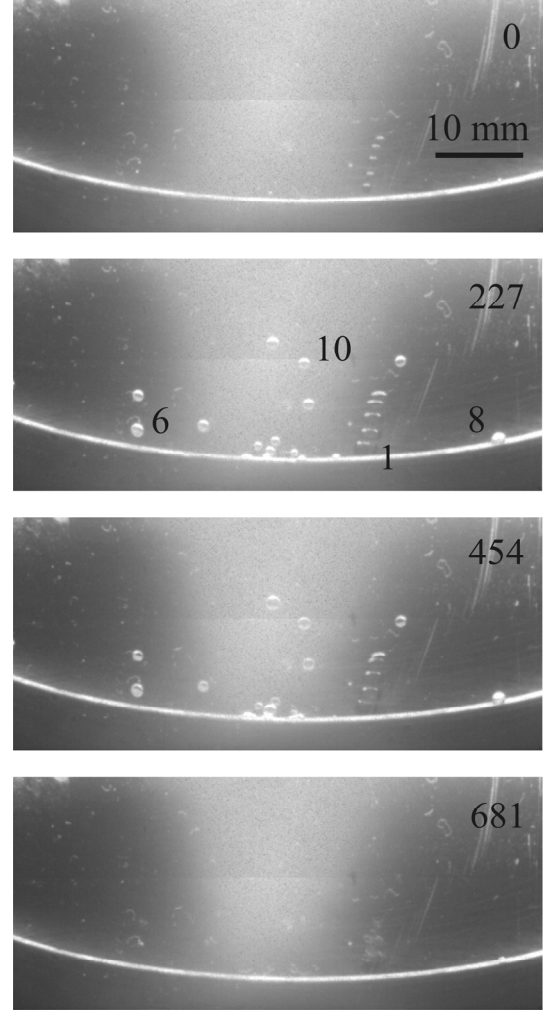


Figure 6. Cavitation caused by the impact of a mass of $m = 0.30 \text{ kg}$ from a height of $h_m = 0.13 \text{ m}$ (impact momentum $P_{imp} = 0.48 \text{ kgm/s}$) onto the end stop of the impact rod, the tube viewed at an oblique angle of 22° with the horizontal plane. The time is indicated in μs in each frame. Bubble 1 is located on the bottom about 15 mm behind and 6 mm to the right of the axis, bubble 6 on the tube wall, bubble 8 on the edge of the spherical bottom, and bubble 10 in the bulk of water.

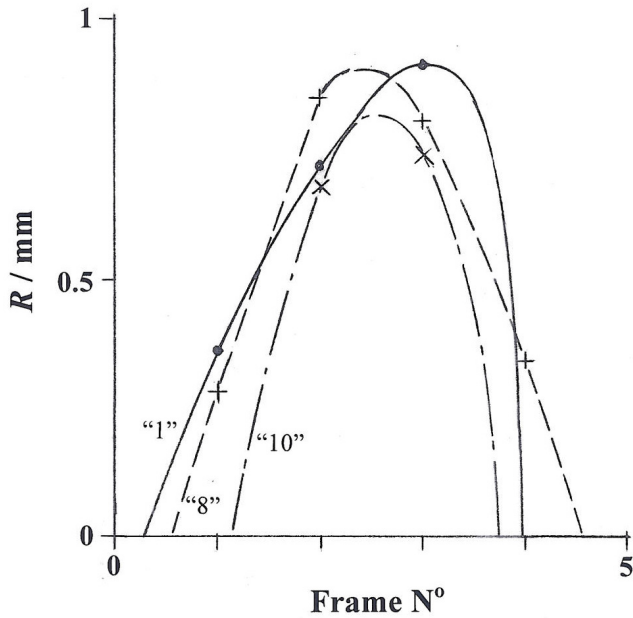


Figure 7. Bubble radii during the initial growth of bubble 1 (•) positioned on the central bottom, bubble 8 (+) positioned on the rim of the bottom, and bubble 10 (×) positioned in the bulk of water. Frame interval 227 μ s.

4. DISCUSSION

The experiments show that the spherically shaped bottom of the device produces a sufficient focusing of the tensile stress pulse to allow the bubbles to be generated in the bulk of water above the bottom. Thus, it allows in situ measurement of the tensile strength. Within a single experiment for example, values of the tensile strength found for 13 individual bubbles, using distilled water from a university supply tap, range from $TS = 0.15$ to $TS = 0.61$ bar, giving a mean tensile strength of $\langle TS \rangle = 0.35$ bar.

It is found that when the intensity of the tensile stress wave is sufficient to cause cavitation in the bulk of liquid, it also sets up cavitation at locations on the spherically shaped bottom where the tensile pulse first reaches the solid-water interface. Here cavitation nuclei of $\langle TS \rangle = 0.08$ bar ($u(TS) = 0.02$ bar) develop into cavities. These cavities defocus the stress wave propagating towards the focal point F , and hereby reduce the efficiency of the system. The tensile strength at the bottom is about 0.3 bar lower than in the bulk of water, a difference which in spite of the uncertainties of measurement is statistically significant, and it is qualitatively in accordance with general observations.

Cavitation is observed in the device for $P_{imp} > 0.42$ kg m/s. This corresponds to an equilibrium velocity of its centre of gravity ~ 0.1 m/s after the impact of the body of mass m . A tensile stress wave of 1.08 bar, calculated from the high-speed video to cause cavitation at the bottom-water interface, has an interface velocity of 0.073 m/s – a difference which we ascribe to the transient motion of the system.

The pressure pulse recordings in [1], measured on the bottom of that system (shown in Figure 1 of the present paper), reveal an initial tensile stress of at least 1 bar, i.e. a much higher tensile strength than we find at the bottom of the present system.

However, in [1] the initial tube acceleration caused total separation between the column of water and the bottom of the accelerated device. We assume that in repeated experiments, a significant degassing of the water has occurred. Further, in each experiment a strong compressive wave is produced at collapse of the separation cavity, followed by multiple compressive pulses, their strength being of the order of 10 bar. These factors are considered responsible for the increased tensile strength, revealed from the pressure recordings in [1].

It is noteworthy that medical piezoelectric lithotripters, operated in normal mode, deliver a leading compressive pulse, of displacement amplitude at the piezo crystals in the range of μ m and with a rise time of less than a μ s, and that apparently cavitation does not occur on the lithotripter surface during the tensile stress that follows. This indicates that the compressive pulse eliminates cavitation nuclei at the solid-water interface. Likewise, the compressive pulse is supposed to raise also the tensile strength of the liquid in the bulk of water as reported in [5-6]. If the pulse is inverted, and starts with a tensile stress pulse, as in the experiments by Professor Crum [9], an amplitude of the piezo crystals of just 0.1 μ m would probably cause cavitation at the crystal surfaces – and it would affect the focusing of the wave. This may explain why the erosive power of Professor Crum's lithotripter was lost at pulse inversion, but no information is available to the authors of the amplitude of the inverted pulse actually used. An investigation of the tensile strength of liquids exposed to compressive pulses remains to be carried out, and design of a mechanical as well as a piezoelectric device for the purpose are in progress.

ACKNOWLEDGMENT

The authors thank Mr. Erik Hansen for his careful construction of the experimental set up.

REFERENCES

- [1] Mørch, K. A. 1982 Energy considerations on the collapse of cavity clusters. *Applied Scientific Research* **38**, 313-321.
- [2] Briggs, L. J. 1950 Limiting negative pressure in water. *Journal of Applied Physics* **21**, 721-722.
- [3] Keller, A. P. 1980 Schlussbericht über das Forschungsvorhaben "Beginnende Kavitation, Zugspannungen in Flüssigkeiten". Technischen Universität München.
- [4] Mørch, K. A. 2009 Cavitation Nuclei: Experiments and Theory. *Journal of Hydrodynamics* **21**, 176-189.
- [5] Borkent, B. M., Arora, M., Ohl, C.-D., de Jong, N., Versluis, M., Lohse, D., Mørch, K. A., Klaseboer, E. and Khoo, B. C. 2008 The acceleration of solid particles subjected to cavitation nucleation. *Journal of Fluid Mechanics* **610**, 157-182.
- [6] Arora, M., Ohl, C.-D. and Mørch, K. A. 2004 Cavitation Inception on Microparticles: A Self-Propelled Particle Accelerator. *Physical Review Letters* **92**, 174501.
- [7] Marschall, H. B., Mørch, K. A., Keller, A. P. and Kjeldsen, M. 2003 Cavitation inception by almost spherical solid particles in water. *Physics of Fluids* **15**, 545-553.
- [8] Mørch, K. A. 2009 Cavitation Nuclei: Experiments and Theory. WIMRC Cavitation Forum 2008.
- [9] Crum, L. A. Conference discussion WIMRC Cavitation Forum 2008.

On the fundamental equations of two-dimensional bubbly cavitating flows

Can F. Delale, Işık University 34980 Şile, İstanbul, Turkey

delale@isikun.edu.tr

ABSTRACT

A bubbly flow model, which couples the Euler equations of motion to spherical bubble dynamics is considered as a non-barotropic model of cavitating flows. By scale separation, evolution equations are obtained for the bubble radius and for the flow velocity, the latter being determined by an integro-partial differential system for the unsteady acceleration. More importantly, this integro-algebraic partial differential system seems to form the fundamental transport equations for the dilation and vorticity. In particular, the transport equation of vorticity is shown to be precisely Fridman's equation of vorticity, containing terms arising from the baroclinic torque of non-barotropic flow. As an application, the initial and boundary value problem of the evolution equations is then discussed for cavitating flows in converging-diverging nozzles and a numerical method to integrate the equations is introduced. The mixture pressure, density and void fraction are then universally (independent of flow dimensionality) related to the solution of the evolution system. The procedure generalizes the quasi-one-dimensional bubbly cavitating nozzle flow solution of Delale et al. [1].

NOMENCLATURE

Latin

H	=	height of nozzle
R	=	bubble radius
Re	=	flow Reynolds number
S	=	surface tension coefficient
U	=	flow speed
L	=	micro to macro scale
k	=	polytropic exponent
p	=	mixture pressure
t	=	time coordinate
x	=	nozzle axial coordinate
y	=	nozzle
u	=	x-component of velocity field
v	=	y-component of velocity field
a	=	x-component of unsteady acceleration field
b	=	y-component of unsteady acceleration field

Greek

β	=	void fraction
μ_{eff}	=	effective viscosity of liquid
η_0	=	number density of nuclei per unit liquid volume
ρ	=	mixture density
ψ	=	dilation
ω	=	vorticity
κ_0	=	parameter in terms of initial void fraction
Λ	=	bubble-bubble interaction parameter

Subscripts

e	=	nozzle exit
g	=	gas
i	=	nozzle inlet
o	=	initial
ℓ	=	liquid phase
v	=	vapor phase

Superscripts

$'$	=	signifies a dimensional quantity (otherwise dimensionless)
-----	---	--

1. INTRODUCTION

Cavitating flows have direct applications in ducts, in venturi tubes, in Diesel injection nozzles, in hydraulic turbomachinery and in the ship industry. Their understanding and modeling in different geometries is still a forbidden problem. The first two-phase bubbly liquid flow model through a converging-diverging nozzle was proposed by Tangren et al. [2] using a barotropic model. The problem has been reconsidered by Ishii et al. [3] by taking into account unsteady effects, but still neglecting bubble dynamics. A one-dimensional continuum bubbly flow model that couples spherical bubble dynamics to the flow equations was proposed by van Wijngaarden [4] and was later employed in the investigation of shock wave structure by Noordzij & van

Wijngaarden [5]. Quasi-one-dimensional steady-state solutions of bubbly cavitating flows through converging-diverging nozzles have also been investigated using the continuum bubbly mixture model (Wang & Brennen [6]; Delale et al. [7]) by assuming that the gas pressure inside the bubble obeys the polytropic law and by lumping all damping mechanisms by a single damping coefficient in the form of viscous dissipation. These investigations have demonstrated that steady-state solutions are possible only for some range of the cavitation number, with the rest of the parameters kept fixed. Moreover, a recent investigation by Pasinlioglu et al. [8] shows that the temporal stability of these quasi-one-dimensional steady-state solutions suffer from being very sensitive to slight unsteady perturbations. A numerical investigation of unsteady quasi-one-dimensional bubbly cavitating flows has already been investigated by Preston et al. [9], showing the possibility of propagating bubbly shock waves in the diverging section of the nozzle. However, unsteady quasi-one-dimensional flow solutions are unsatisfactory in describing the multi-dimensional structures of cavitating flows.

The aim of this investigation is to give a detailed analysis of two-dimensional cavitating flows using a non-barotropic model. In this context we discuss a modified version of the bubbly flow model of van Wijngaarden [4] and reduce the system of model equations to evolution equations for the bubble radius and flow velocity, the latter being determined by an integro-partial differential system for the unsteady acceleration. More importantly, this integro-partial differential system seems to form the fundamental transport equations of the dilation and vorticity in cavitating flows. In particular, the transport equation of vorticity is shown to be precisely Fridman's equation of vorticity (see Saffman [10]), containing terms arising from non-barotropic flow. The initial and boundary value problem of the evolution equations are then discussed for cavitating flows in converging-diverging nozzles and a method to integrate the equations is introduced.

2. THE BUBBLY FLOW MODEL AND TWO-DIMENSIONAL FORMULATION

We consider an unsteady two-dimensional bubbly cavitating flow and we assume that, for a given geometric configuration, the initial distributions and the boundary conditions are such that cavitation can occur within the flow. We use a slightly modified version of the two-phase homogeneous bubbly mixture model of van Wijngaarden [4], which couples the unsteady flow equations to spherical bubble dynamics. This model has already been employed by Wang and Brennen [6] and by Delale et al. [7] for the investigation of quasi-one-dimensional steady-state cavitating nozzle flows, and by Preston et al. [9] for quasi-one-dimensional unsteady cavitating nozzle flows. In this model the slip between the bubbles and the liquid as well as the creation (nucleation and bubble fission) and coagulation of bubbles are neglected and spherical bubbles are assumed. These assumptions have been specifically addressed [11-19] and improvements on these assumptions can be taken into

account by an improved model. The two-dimensional unsteady cavitating flow equations then take the form

$$\rho' = \rho'_\ell(1 - \beta), \quad (1)$$

$$\frac{\partial \rho'}{\partial t'} + \frac{\partial}{\partial x'}(\rho' u') + \frac{\partial}{\partial y'}(\rho' v') = 0, \quad (2)$$

$$\rho' \left(\frac{\partial u'}{\partial t'} + u' \frac{\partial u'}{\partial x'} + v' \frac{\partial u'}{\partial y'} \right) = - \frac{\partial p'}{\partial x'}, \quad (3)$$

$$\rho' \left(\frac{\partial v'}{\partial t'} + u' \frac{\partial v'}{\partial x'} + v' \frac{\partial v'}{\partial y'} \right) = - \frac{\partial p'}{\partial y'} \quad (4)$$

and

$$\frac{R'^3(1 - \beta)}{\beta} = \frac{3}{4\pi\eta'_0} = \text{constant}. \quad (5)$$

In eqs. (1)-(5), ρ' is the mixture density where the contribution from the dispersed gaseous phase has been neglected, ρ'_ℓ is the liquid density, p' is the mixture pressure, β is the void fraction, (u', v') are the cartesian components of the two-dimensional velocity field and R' is the spherical bubble radius with η'_0 denoting the number of bubbles per unit volume of the liquid phase. Furthermore, (x', y') denote the cartesian coordinates of the two-dimensional flow field and t' denotes the time. It is also worthwhile to note that, in the momentum eqs. (3) and (4), the viscous and gravity terms are neglected. The above equations are supplemented by a modified Rayleigh-Plesset equation for spherical bubble dynamics, which takes bubble/bubble interactions into account in the mean-field as [7]

$$\begin{aligned} \frac{p'_v - p'}{\rho'_\ell} &= \frac{[1 + (2/3)\pi\eta'_0(3\Lambda^2 - 1)R'^3]}{[1 + (4/3)\pi\eta'_0R'^3]^2} R' \frac{d^2 R'}{dt'^2} \\ &+ \frac{3}{2} \frac{[1 + (8/3)\pi\eta'_0(2\Lambda^2 - 1)R'^3 + (16/9)\pi^2\eta'^2_0\Lambda^2 R'^6]}{[1 + (4/3)\pi\eta'_0R'^3]^2} \left(\frac{dR'}{dt'} \right)^2 \\ &+ \frac{2S'}{\rho'_\ell R'} + \frac{4\mu'_{eff}}{\rho'_\ell R'} \frac{dR'}{dt'} - \frac{p'_{g0}}{\rho'_\ell} \left(\frac{R'_0}{R'} \right)^{3k} \end{aligned} \quad (6)$$

where $d/dt' = \partial/\partial t' + u' \partial/\partial x' + v' \partial/\partial y'$ denotes the material or total derivative, S' is the surface tension coefficient, Λ denotes the bubble/bubble interaction parameter defined by

$$\Lambda = \frac{\Delta r'}{R'} \quad (7)$$

with $\Delta r'$ denoting the radius of influence of interacting bubbles from the center of any fixed bubble [7,20]. In eq. (6) a polytropic law, with index k , is assumed for the expansion and compression of the gas inside the gas/vapor bubble with p'_v and p'_{g0} denoting, respectively, the constant partial vapour pressure and the initial value of the partial gas pressure, and all damping mechanisms, in an *ad hoc* manner, [21-24] are assumed in the form of viscous dissipation, characterized by a single viscosity coefficient μ'_{eff} . Equations (1)-(7) constitute the model equations for unsteady 2-D bubbly cavitating flows. Using the normalization

$$\begin{aligned} \rho &= \frac{\rho}{\rho'_\ell}, \quad p = \frac{p'}{p'_0}, \quad p_v = \frac{p'_v}{p'_0}, \quad p_g = \frac{p'_g}{p'_0} \\ u &= \frac{u'}{\sqrt{p'_0 / \rho'_\ell}}, \quad v = \frac{v'}{\sqrt{p'_0 / \rho'_\ell}}, \quad R = \frac{R'}{R'_0} \\ x &= \frac{x'}{H'}, \quad y = \frac{y'}{H'}, \quad t = \frac{\sqrt{p'_0 / \rho'_\ell} t'}{H'} \end{aligned} \quad (8)$$

where H' is a characteristic flow length, R'_0 is a characteristic bubble radius and p'_0 is a reference pressure (the latter two usually obtained from the specified from the initial distributions), the two-dimensional normalized model equations take the form

$$\rho = 1 - \beta, \quad (9)$$

$$\frac{\partial \rho}{\partial t} + \frac{\partial}{\partial x}(\rho u) + \frac{\partial}{\partial y}(\rho v) = 0, \quad (10)$$

$$\rho \left(\frac{\partial u}{\partial t} + u \frac{\partial u}{\partial x} + v \frac{\partial u}{\partial y} \right) = - \frac{\partial p}{\partial x}, \quad (11)$$

$$\rho \left(\frac{\partial v}{\partial t} + u \frac{\partial v}{\partial x} + v \frac{\partial v}{\partial y} \right) = - \frac{\partial p}{\partial y} \quad (12)$$

and

$$R^3 \frac{1 - \beta}{\beta} = \frac{1 - \beta_0}{\beta_0} = \kappa_0^3 \quad (13)$$

where β_0 is a characteristic initial void fraction. The system of model equations (9)-(13) is completed by the normalized modified Rayleigh-Plesset equation, given by

$$\begin{aligned} \frac{p_v - p}{L^2} &= \frac{[1 + (3\Lambda^2 - 1)(R / \kappa_0)^3 / 2]}{[1 + (R / \kappa_0)^3]} R \frac{d^2 R}{dt^2} \\ &+ \frac{3}{2} \frac{[1 + 2(2\Lambda^2 - 1)(R / \kappa_0)^3 + \Lambda^2 (R / \kappa_0)^6]}{[1 + (R / \kappa_0)^3]^2} \left(\frac{dR}{dt} \right)^2 \\ &+ \frac{S_0}{L^2 R} + \frac{4}{L^2 (\text{Re}) R} \frac{dR}{dt} - \frac{p_{g0}}{L^2 R^{3k}} \end{aligned} \quad (14)$$

where L is the ratio of micro scale to macro scale defined by

$$L = \frac{R'_0}{H'}, \quad (15)$$

κ_0 is a parameter defined in terms of the characteristic initial void fraction β_0 by

$$\kappa_0^3 = \frac{1 - \beta_0}{\beta_0}, \quad (16)$$

S_0 is the non-dimensional surface tension coefficient defined by

$$S_0 = \frac{2S'}{p'_0 R'_0}, \quad (17)$$

and Re is a typical Reynolds number, based on the overall damping coefficient μ'_{eff} , and is defined by

$$\text{Re} = \frac{\rho'_\ell H' \sqrt{p'_0 / \rho'_\ell}}{\mu'_{eff}}. \quad (18)$$

2.1 Evolution Equations for the Velocity Field and Bubble Radius in Two Dimensions

In this section we eliminate the normalized mixture density ρ and the void fraction β using the algebraic relations (9) and (13) in the normalized continuity equation (10), and the normalized pressure field between the normalized modified Rayleigh-Plesset equation (14) and the normalized momentum equations (11) and (12). We then arrive at the following system of evolution equations for the normalized radius R and the normalized velocity field (u, v) as

$$\frac{\partial R}{\partial t} = \frac{R^3 + \kappa_0^3}{3R^2} \left(\frac{\partial u}{\partial x} + \frac{\partial v}{\partial y} \right) - u \frac{\partial R}{\partial x} - v \frac{\partial R}{\partial y}, \quad (19)$$

$$\frac{\partial u}{\partial t} = a \quad (20)$$

and

$$\frac{\partial v}{\partial t} = b \quad (21)$$

where the unsteady acceleration field (a, b) satisfies the following linear system of partial differential equations:

$$\begin{aligned} & \frac{\partial^2 a}{\partial x \partial y} + \frac{\partial^2 b}{\partial y^2} + \frac{2[(3\Lambda^2 - 1)(R/\kappa_0)^3 - 1]}{R[2 + (3\Lambda^2 - 1)(R/\kappa_0)^3]} \frac{\partial R}{\partial y} \left(\frac{\partial a}{\partial x} + \frac{\partial b}{\partial y} \right) \\ & - \frac{6R}{L^2 \kappa_0^3 [2 + (3\Lambda^2 - 1)(R/\kappa_0)^3] [1 + (R/\kappa_0)^3]} b = \bar{S}_a \end{aligned} \quad (22)$$

and

$$\frac{\partial b}{\partial x} - \frac{\partial a}{\partial y} - \frac{3R^2}{R^3 + \kappa_0^3} \left(\frac{\partial R}{\partial x} b - \frac{\partial R}{\partial y} a \right) = S_b \quad (23)$$

and where \bar{S}_a and S_b are defined by

$$\begin{aligned} \bar{S}_a = & - \left(u \frac{\partial}{\partial x} + v \frac{\partial}{\partial y} \right) \frac{\partial \psi}{\partial y} - \frac{\partial u}{\partial y} \frac{\partial \psi}{\partial x} - \frac{\partial v}{\partial y} \frac{\partial \psi}{\partial y} \\ & + \left\{ \frac{1}{[1 + (R/\kappa_0)^3]} \left(u \frac{\partial v}{\partial x} + v \frac{\partial v}{\partial y} \right) + \frac{\partial p_v}{\partial y} \right\} \\ & \times \frac{6R}{L^2 \kappa_0^3 [2 + (3\Lambda^2 - 1)(R/\kappa_0)^3]} \\ & - \left\{ \frac{2\kappa_0^3 [(6\Lambda^2 - 1)(R/\kappa_0)^6 + (6\Lambda^2 - 2)(R/\kappa_0)^3 - 1]}{3R^3} \psi \right. \\ & \left. + \frac{8[1 + (R/\kappa_0)^3]}{L^2 (\text{Re}) R^2} \right\} \left\{ \frac{1}{[2 + (3\Lambda^2 - 1)(R/\kappa_0)^3]} \frac{\partial \psi}{\partial y} \right. \\ & \left. + \frac{1}{[2 + (3\Lambda^2 - 1)(R/\kappa_0)^3]} \right\} \\ & \times \left\{ \frac{6S_0}{L^2 \kappa_0^3 R} - \frac{18kp_{g0}}{L^2 \kappa_0^3 R^{3k}} + \frac{24}{L^2 (\text{Re}) R^3} \psi \right. \end{aligned}$$

$$\begin{aligned} & - \frac{2}{R} [(3\Lambda^2 - 1)(R/\kappa_0)^3 - 1] \left(u \frac{\partial \psi}{\partial x} + v \frac{\partial \psi}{\partial y} \right) \\ & - \frac{2\kappa_0^3 [(6\Lambda^2 - 1)(R/\kappa_0)^6 - (3\Lambda^2 - 1)(R/\kappa_0)^3 + 2]}{3R^4} \psi^2 \left\{ \frac{\partial R}{\partial y} \right\} \end{aligned} \quad (24)$$

and

$$\begin{aligned} S_b = & -\omega \psi - u \frac{\partial \omega}{\partial x} - v \frac{\partial \omega}{\partial y} \\ & + \frac{3R^2}{(R^3 + \kappa_0^3)} \left[\left(u \frac{\partial v}{\partial x} + v \frac{\partial v}{\partial y} \right) \frac{\partial R}{\partial x} - \left(u \frac{\partial u}{\partial x} + v \frac{\partial u}{\partial y} \right) \frac{\partial R}{\partial y} \right] \end{aligned} \quad (25)$$

In eqs. (24) and (25), ψ and ω , respectively, denote the dilation (the divergence of the velocity field) and the vorticity and are given by

$$\psi = \frac{\partial u}{\partial x} + \frac{\partial v}{\partial y} \quad (26)$$

and

$$\omega = \frac{\partial v}{\partial x} - \frac{\partial u}{\partial y}. \quad (27)$$

In particular, by integration by parts, eq. (22) together with eq. (24) can be transformed into a first order linear integro-partial differential equation for the unsteady acceleration field. Equations (22) and (23) then become

$$\begin{aligned} & \frac{\partial a}{\partial x} + \frac{\partial b}{\partial y} - \frac{R[2 + (3\Lambda^2 - 1)(R/\kappa_0)^3]}{R_1[2 + (3\Lambda^2 - 1)(R/\kappa_0)^3]} \left(\frac{\partial a}{\partial x} + \frac{\partial b}{\partial y} \right)_{y=0} \\ & - \frac{6R}{L^2 \kappa_0^3 [2 + (3\Lambda^2 - 1)(R/\kappa_0)^3]} \int_0^y \frac{b}{[1 + (R/\kappa_0)^3]} dy_1 = S_a \end{aligned} \quad (28)$$

and

$$\frac{\partial b}{\partial x} - \frac{\partial a}{\partial y} - \frac{3R^2}{R^3 + \kappa_0^3} \left(\frac{\partial R}{\partial x} b - \frac{\partial R}{\partial y} a \right) = S_b \quad (29)$$

where $R_I = R(x, 0, t)$ and the source term S_a is now given by

$$\begin{aligned}
S_a = & - \left(u \frac{\partial \psi}{\partial x} + v \frac{\partial \psi}{\partial y} \right) \\
& + \frac{R \left[2 + (3\Lambda^2 - 1)(R/\kappa_0)^3 \right]}{R_1 \left[2 + (3\Lambda^2 - 1)(R/\kappa_0)^3 \right]} \left(u \frac{\partial \psi}{\partial x} + v \frac{\partial \psi}{\partial y} \right)_{y=0} \\
& + \frac{R}{\left[2 + (3\Lambda^2 - 1)(R/\kappa_0)^3 \right]} \int_0^y \mathbf{s}_a \, dy_1
\end{aligned} \tag{30}$$

with the integrand \mathbf{S}_a , in eq. (30), defined by

$$\begin{aligned}
\mathbf{s}_a = & \frac{6}{L^2 \kappa_0^3 \left[1 + (R/\kappa_0)^3 \right]} \left(u \frac{\partial v}{\partial x} + v \frac{\partial v}{\partial y} \right) + \frac{6}{L^2 \kappa_0^3} \frac{\partial p_v}{\partial y} \\
& - \left\{ \frac{2\kappa_0^3 \left[(6\Lambda^2 - 1)(R/\kappa_0)^6 + (6\Lambda^2 - 2)(R/\kappa_0)^3 - 1 \right]}{3R^4} \right\} \psi \\
& + \frac{8 \left[1 + (R/\kappa_0)^3 \right]}{L^2 (\text{Re}) R^3} \left\{ \frac{\partial \psi}{\partial y} \right. \\
& + \left\{ \frac{6S_0}{L^2 \kappa_0^3 R^2} - \frac{18kp_{g0}}{L^2 \kappa_0^3 R^{3k+1}} + \frac{24}{L^2 (\text{Re}) R^4} \right\} \psi \\
& \left. - \frac{2\kappa_0^3 \left[(6\Lambda^2 - 1)(R/\kappa_0)^6 - (3\Lambda^2 - 1)(R/\kappa_0)^3 + 2 \right]}{3R^5} \right\} \psi^2 \left\{ \frac{\partial R}{\partial y} \right\}.
\end{aligned} \tag{31}$$

2.2 Transport Equations for the Dilation and Vorticity

Equations (28) and (29) for the unsteady acceleration field (a , b) constitute the fundamental equations for the transport of the dilation ψ and of the vorticity ω in 2D bubbly cavitating flows. In particular, eq. (29) can be shown to be precisely the non-barotropic vorticity transport equation, called the Fridman equation [10], given by

$$\frac{\partial \bar{\omega}}{\partial t} + (\bar{\mathbf{u}} \cdot \bar{\nabla}) \bar{\omega} = \bar{S}_c = -\psi \bar{\omega} + (\bar{\omega} \cdot \bar{\nabla}) \bar{\mathbf{u}} + \frac{1}{\rho^2} \bar{\nabla} \rho \times \bar{\nabla} p \tag{32}$$

where $\bar{\omega} = \omega \bar{\mathbf{k}}$, with $\bar{\mathbf{k}}$ denoting the unit normal vector perpendicular to the x - y plane, and where the second term $(\bar{\omega} \cdot \bar{\nabla}) \bar{\mathbf{u}}$ on the right-hand side of the equation vanishes in 2D. Equation (32) forms the basis for the generation of

vorticity in non-barotropic flows. Moreover, the first term on the right hand side of eq. (32) characterizes the effect of compressibility whereas the third term is the baroclinic torque arising from the non-barotropic character of the flow. Similarly, eq. (28) together with the source term given by eqs. (30) and (31) can be written as a transport equation for the dilation ψ , i.e.

$$\frac{\partial \psi}{\partial t} + (\bar{\mathbf{u}} \cdot \bar{\nabla}) \psi = S_d, \tag{33}$$

arising mainly due to the compressibility effect of cavitating flows where the source term S_d can be identified from eqs. (28) and (30). The transport eqs. (32) and (33) are responsible for the formation of the re-entrant jet in partial cavitation and for all closure models of cavitation. *In the absence of cavitation where the source terms S_a and S_b vanish, eqs. (28) and (29) reduce to the classical Cauchy-Riemann equations (existence of the complex velocity potential), as expected.*

2.3 The Pressure-Dilation Relation

The evolution eqs. (19)-(21) for the bubble radius and velocity fields together with the linear integro-partial differential system (28)-(31) for the unsteady acceleration field has to be supplemented by initial and boundary conditions of the bubble radius and of the velocity field for a given geometric configurational domain. The evolution eqs. (19)-(21) can then be solved for the bubble radius and velocity fields, from which the dilation ψ and the vorticity ω can be calculated. The mixture pressure, the void fraction and the density then follow by

$$\begin{aligned}
p = & p_v - \frac{S_0}{R} + \frac{p_{g0}}{R^{3k}} \\
& - \frac{L^2 \kappa_0^6}{18R^4} \left[(6\Lambda^2 - 1)(R/\kappa_0)^6 \right. \\
& \left. + (6\Lambda^2 - 2)(R/\kappa_0)^3 - 1 \right] \psi^2 \\
& - \frac{4\kappa_0^3}{3(\text{Re})R^3} \left[1 + (R/\kappa_0)^3 \right] \psi \\
& - \frac{L^2 \kappa_0^3}{6R} \left[2 + (3\Lambda^2 - 1)(R/\kappa_0)^3 \right] \frac{d\psi}{dt}
\end{aligned} \tag{34}$$

and

$$\beta = 1 - \rho = \frac{R^3}{R^3 + \kappa_0^3}. \tag{35}$$

Equation (35) relates the density field and the void fraction to the solution of the bubble radius whereas eq. (34) relates the pressure to the bubble radius, the dilation and its total derivative. In particular equation (34), which is based on the modified Rayleigh-Plesset equation of spherical bubble

dynamics, constitutes a fundamental relation between the mixture pressure and the dilation (the compressibility effect of the flow). It is independent of flow dimensionality and may be helpful for a quantitative comparison of the pressure distributions obtained by different cavitation models, whether they are based on barotropic relations or phase transition models. For incompressible flow ($\psi = 0$), it reduces to the local mechanical equilibrium condition (Laplace's equation)

$$p = p_v - \frac{S_0}{R} + \frac{P_{g0}}{R^{3k}}. \quad (36)$$

The steady-state solution of the model equations are obtained if, in addition to the vanishing of the unsteady acceleration ($a = b = 0$), $\partial R / \partial t$ also vanishes everywhere for all times. In such a case we obtain the two-dimensional steady-state solution.

3. THE INITIAL/BOUNDARY VALUE PROBLEM OF THE EVOLUTION EQUATIONS FOR TWO-DIMENSIONAL CAVITATING NOZZLE FLOWS AND METHOD OF SOLUTION

In order to discuss the solution of the two-dimensional system of evolution equations (19)-(21) of the bubble radius and of the flow velocity field for cavitating flows, we discuss an application in nozzle flows for which unsteady quasi-one-dimensional solutions are already available[1,9]. For this reason we consider a two-dimensional converging-diverging nozzle whose geometric configuration is shown in Fig. 1. In this case the length of the nozzle is elongated in both the inlet and exit directions with corresponding constant inlet and exit areas to ensure uniform inlet and exit boundary conditions across the cross-sectional areas at the inlet and exit of the nozzle. We also choose the normalized inlet height to be unity for normalization. We let the nozzle axis coincide with the x -axis and the transverse perpendicular direction be parallel to the y -axis with origin on the nozzle axis at the inlet. We also assume a symmetric configuration of the flow field with respect to the x -axis ($y=0$) so that it is sufficient to discuss the solution in the upper symmetric domain of the nozzle. We choose the appropriate inlet and exit conditions in such a way that cavitation (attached partial cavitation or supercavitation) occurs within the nozzle. It is also worthwhile to mention that, in specifying the initial distributions of the bubble radius and of the velocity field for the evolution equations, care should be taken to start with irrotational flow in order to access the correct order of magnitude of vorticity generated in the cavitating regime. With these mind, we choose the initial flow field to be irrotational everywhere in the computational domain

$$u(x, y, 0) = u_0(x, y) \text{ and } v(x, y, 0) = v_0(x, y) \quad (37)$$

and also uniform and uni-directional ($v_0=0$) at the nozzle inlet and exit (i.e., at $x=x_i$ and $x=x_e$).

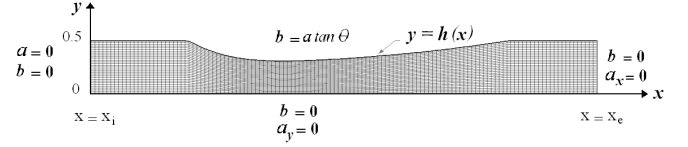


Fig. 1: Nozzle geometry and boundary conditions of the unsteady acceleration field for two-dimensional bubbly cavitating nozzle flows.

We also choose the initial bubble radius distribution

$$R(x, y, 0) = R_0(x, y) \quad (38)$$

in such a way that it is uniform at the nozzle inlet and exit. Taking into account the hyperbolicity of eq. (19) for the bubble radius for a given velocity field, we need only to specify the bubble radius at the inlet. Assuming that the inlet bubble radius distribution is uniform over the cross-sectional area at all times, we have

$$R(x_i, y, t) = R_i(t) \quad (39)$$

with $R_i(0)$ being equal to the corresponding initial inlet bubble radius to avoid a discontinuity in the bubble radius at the nozzle inlet. In particular, we choose $R_i(0)=1$ for normalization. For the flow velocity and mixture pressure, we can specify two sets of boundary conditions:

(a) *The inlet flow speed and exit pressure, both uniform over the cross-sectional area, are specified, i.e.*

$$u(x_i, y, t) = U_i(t), v(x_i, y, t) = 0 \text{ and } p(x_e, y, t) = P_e(t) \quad (40)$$

for $t \geq 0$ together with $U_i(0)$ and $P_e(0)$ matching the corresponding initial inlet and exit values to ensure continuity of the solutions.

(b) *The inlet and exit pressures, both uniform over the cross-sectional area, are specified, i.e.*

$$p(x_i, y, t) = P_i(t) \text{ and } p(x_e, y, t) = P_e(t) \quad (41)$$

for $t \geq 0$ together with $P_i(0)$ and $P_e(0)$ matching the corresponding initial inlet and exit values to ensure continuity of the solutions. In particular, we choose $P_i(0)=1$ for normalization.

The above boundary conditions, similar to the procedure in quasi-one-dimensional flows [1], should be converted to the boundary conditions of the unsteady acceleration field for the integro-partial differential system, given by eqs. (28) and (29). For this reason, assuming that the inlet velocity field is uniform, constant and uni-directional for case (a) and that the bubbles are in mechanical equilibrium at the exit of the nozzle, as well as at the inlet for case (b), we can arrive at the following boundary conditions for the system of eqs. (28) and (29) in each case :

Case (a) The inlet flow speed and exit pressure are specified.

$$\begin{aligned} a=0 \text{ and } b=0 \text{ at } x=x_i, \quad a_x=0 \text{ and } b=0 \text{ at } x=x_e, \\ a_y=0 \text{ and } b=0 \text{ at } y=0, \quad b=a \tan \theta \text{ at } y=h(x) \end{aligned} \quad (42)$$

where $y=h(x)$ denotes the shape of the upper wall of the nozzle and $\tan \theta = dh/dx$. Such a configuration of the boundary conditions are given in Fig. 1.

Case (b) The inlet and exit pressures are specified.

$$\begin{aligned} a_x=0 \text{ and } b=0 \text{ at } x=x_i, \quad a_x=0 \text{ and } b=0 \text{ at } x=x_e, \\ a_y=0 \text{ and } b=0 \text{ at } y=0, \quad b=a \tan \theta \text{ at } y=h(x). \end{aligned} \quad (43)$$

For the numerical method, similar to the procedure for quasi-1D flows, we first consider the integro-partial differential system of equations, given by eqs. (28) and (29), subject to boundary conditions given by either eq. (42) or eq. (43). The system is solved in two iterative steps. In the first step the integral on the left-hand side of eq. (28) is set equal to zero and the remaining elliptic system of first order partial differential equations is first discretized by a central finite difference scheme. The resulting linear system of algebraic equations, subject to the boundary conditions given in eq. (28) or in eq. (29), are solved by Gauss-Seidel Over Relaxation Method. In the second step, the skipped integral on the left hand side of eq. (28) is evaluated and treated as a source term. The first step is then repeated to obtain the unsteady acceleration field at that instant. The iterative procedure is continued until convergence of the solution is achieved. Using a multi-stage Runge-Kutta method in time and the solution for the unsteady acceleration field, the evolution eqs. (20) and (21) are integrated to yield the velocity field in the next time step. To obtain the bubble radius in the next stage, we first note that the evolution equation (19) can be transformed into a linear first order partial differential equation using the transformation

$$\chi = \ln \left[R^3 + \kappa_0^3 \right] \quad (44)$$

to arrive at

$$\frac{\partial \chi}{\partial t} + u \frac{\partial \chi}{\partial x} + v \frac{\partial \chi}{\partial y} = \psi(x, y, t) = \frac{\partial u}{\partial x} + \frac{\partial v}{\partial y} \quad (45)$$

Using the velocity field obtained, the hyperbolic equation (45) can be integrated by the method of characteristics or by using flux splitting methods to arrive at the bubble radius in the next time step. The numerical scheme is then repeated for all subsequent time steps.

4. CONCLUSIONS AND FUTURE PERSPECTIVES

Model equations for two-dimensional bubbly cavitating nozzle flows are presented and the evolution equations for the bubble radius and the velocity field are obtained. In particular, the integro-partial differential system of equations for the unsteady acceleration field is shown to constitute the fundamental equations of 2D cavitating flows, exhibiting the evolution of the dilation and of the vorticity. The initial/boundary value problem for two-dimensional bubbly cavitating nozzle flows are then formulated. For quantitative results of two-dimensional bubbly cavitating nozzle flows, an algorithm of the method summarized in section 3 needs to be constructed. Care should be taken to describe the initial distributions to avoid unnecessarily lengthy computational time. Improvements on the model equations have to be considered afterwards.

REFERENCES

- [1] Delale, C.F., Başkaya, Z., S.J.Schmidt, S.J and Schnerr, G.H., 2009 "Unsteady Bubbly Cavitating Nozzle Flows," CAV2009 Seventh International Symposium on Cavitation Paper No. : 18, 17-22 August 2009, Ann Arbor, Michigan, USA .
- [2] Tangren, R.F., Dodge, C.H. , Seifert, H.S.,1949,"Compressibility effects in two-phase flow," J. Appl. Phys. **20**, 637-645.
- [3] Ishii, R., Umeda, Y., Murata, S. and Shishido, N., 1993,"Bubbly flows through a converging-diverging nozzle," Phys. Fluids A **5**, 1630-1643.
- [4] van Wijngaarden, L., 1968, "On the equations of motion for mixtures of liquid and gas bubbles," J. Fluid Mech. **33**, 465-474.
- [5] Noordzij, L. and van, Wijngaarden, L., 1974, "Relaxation effects, caused by the relative motion, on shock waves in gas-bubble/liquid mixtures," J. Fluid Mech. **66**, 115-143.
- [6] Wang, Y. C., and Brennen, C. E., 1998, "One Dimensional Bubbly Cavitating Flows Through a Converging-Diverging Nozzle," ASME J. Fluids Eng., **120**, pp. 166–170.
- [7] Delale, C. F., Schnerr, G. H., and Sauer, J., 2001, "Quasi-One-Dimensional Steady-State Cavitating Nozzle Flows," J. Fluid Mech., **427**, pp. 167–204.
- [8] Pasinlioglu, S., Delale, C.F. and Schnerr, G.H., 2009, "On the Temporal Stability of Quasi-One-Dimensional Steady-State Bubbly Cavitating Nozzle Flow Solutions, " IMA Journal of Applied Mathematics, **74**, pp. 230-249.
- [9] Preston, A. T., Colonius, T., and Brennen, C. E., 2002, "A Numerical Investigation of Unsteady Bubbly Cavitating Nozzle Flows," Phys. Fluids, **14**, pp. 300–311.
- [10] Saffman, P.G., 1995, Vortex Dynamics, Cambridge University Press, Cambridge.
- [11] Brennen, C.E, 1995, Cavitation and Bubble Dynamics, Oxford University Press, Oxford.

- [12] Franc, J.P. and Michel, J.M., 2004, *Fundamentals of Cavitation*, Kluwer Academic Publishers, Dordrecht, p. 20.
- [13] Wang, Y.C. and Chen, E., 2002, "Effect of Phase Relative Motion on Critical Bubbly Flows Through a Converging-Diverging Nozzle," *Phys. Fluids* **14**, 3215-3223.
- [14] Mørch, K. A., 2000, "Cavitation Nuclei and Bubble Formation: A Dynamic Liquid-Solid Interface Problem," *ASME J. Fluids Eng.*, **122**, pp. 494-498.
- [15] Delale, C. F., Hruby J., and Marsik, F., 2003, "Homogeneous Bubble Nucleation in Liquids: The Classical Theory Revisited," *J. Chem. Phys.*, **118**, pp. 792-906.
- [16] Delale, C. F., Okita K., and Matsumoto, Y., 2005, "Steady-State Cavitating Nozzle Flows with Nucleation," *ASME J. Fluids Eng.*, **127**, pp. 770-777.
- [17] Brennen, C.E., 2002, "Fission of Collapsing Cavitation Bubbles," *J. Fluid Mech.*, **472**, 153-166.
- [18] Delale, C. F., and Tunç, M., 2004, "A Bubble Fission Model for Collapsing Cavitation Bubbles," *Phys. Fluids*, **16**, pp. 4200-4203.
- [19] Blake, J.R. and Gibson, D.C., 1987, "Cavitation Bubbles Near Boundaries," *Ann. Rev. Fluid Mech.*, **19**, 99-123.
- [20] Kubota, A., Kato, H. and Yamaguchi, H., 1992, "A numerical study of unsteady cavitation on a hydraulic section," *J. Fluid Mech.* **240**, 59-96
- [21] Nigmatulin, R.I., Khabeev, N.S. and Nagiev, F.B., 1981, "Dynamics, Heat and Mass Transfer of Vapor-Gas Bubbles in a Liquid," *Intl. J. Heat Mass Transfer*, **24**, 1033-1044.
- [22] Prosperetti, A., Crum, L.A. and Commander, K.W., 1988, "Nonlinear bubble dynamics," *J. Acoust. Soc. Am.* **83**, 502-514.
- [23] Prosperetti, A., 1991, "The Thermal Behavior of Oscillating Gas Bubbles," *J. Fluid Mech.*, **222**, 587-616.
- [24] Delale, C. F., 2002, "Thermal Damping in Cavitating Nozzle flows," *ASME J. Fluids Eng.*, **124**, pp. 969-976.

Mathematical modelling of bubble size distribution during acoustic cavitation

Tija Sīle*/University of Latvia
Laboratory for Mathematical Modelling of
Environmental and Technological Processes

Jānis Virbulis/ University of Latvia
Laboratory for Mathematical Modelling
of Environmental and Technological Processes

*tija.sile@gmail.com

ABSTRACT

The calculation of the equilibrium bubble size distribution during acoustic cavitation is an unresolved problem and the bubble equilibrium radius plays an important role in bubble dynamics. Based on a model by Iida et al [1] an extended model of bubble size distribution is proposed. The effects of the acoustic field, rectified diffusion, bubble dissolution, buoyancy rising and bubble coalescence due to the secondary Bjerknes force are considered. The model has one spatial dimension - the distance to the transducer is taken into account. The model is calibrated using experimental data for pulsed ultrasound from literature.

NOMENCLATURE

a - coefficients in the parametrization of the bubble terminal velocity due to buoyancy

C_l - gas concentration in the liquid

C_{sat} - saturation gas concentration in the liquid

c - speed of sound

D - gas diffusion coefficient in the liquid

d - distance between bubbles

f - acoustic field frequency

g - acceleration due to gravity

h - coalescence calibration parameter

k - secondary Bjerknes force related coalescence coefficient

N_b - bubble concentration

N_c - concentration of bubbles that coalesce

n_b - number of bubbles

n_R - number of bubbles changing their radius

n_z - number of bubbles changing their spatial position

P_g - gas pressure

p - pressure

p_∞ - pressure far from the bubble

p_a - acoustic pressure

R - bubble radius

R_0 - equilibrium bubble radius (radius if no acoustic field is applied)

R_g - universal gas constant

R^{cut} - maximal bubble generation radius

S - coalescence probability

T_g - gas temperature

t - time

t_0 - acoustic period

t_{col} - time necessary for two bubbles to coalesce

V - bubble volume

V_{gen} - bubble volume generated

v - bubble velocity

z - spatial coordinate

β_1, β_2 - experimentally determined drag force coefficients

κ - polytropic coefficient

μ - dynamic viscosity coefficient

ν - kinematic viscosity coefficient

ρ_g - gas density

ρ_L - liquid density

σ - surface tension

$\dot{R} = \frac{dR}{dt}$ - time derivative

$\langle x \rangle$ - time averaged value

1. INTRODUCTION

One of the industrial applications of ultrasound is in precision cleaning of semiconductor wafers – megasonic cleaning. There is recent experimental evidence that bubble oscillations have a direct role in the particle removal process [2]. It is well known that the bubble oscillations for a given acoustic field frequency depend on the equilibrium or initial bubble radius – bubble radius in the absence of acoustic field [3 p.10]. The equation describing bubble oscillations is mathematically equivalent to the forced harmonic oscillator equation. Consequently, maximal bubble oscillations occur in the vicinity of a particular bubble radius, called the resonant bubble radius. The resonant bubble radius can be calculated using Minnaert's equation that can be expressed for air bubbles in water as [3 p.9]:

$$f \cdot R_0 = 3 \frac{m}{s}, \quad (1)$$

where *f* is the acoustic field frequency.

Therefore, in order to optimize the cleaning process it is necessary to have information about the bubble size distribution. Many processes has been studied in detail – bubble oscillations [3], bubble movement due to an acoustic field (primary Bjerknes force [4] and bubble–bubble interaction (secondary Bjerknes force) in an acoustic field [5]. However, up to authors' knowledge, no theoretical model for the bubble size distribution during the action of an acoustic field has been proposed yet.

The experimental results regarding bubble size distribution have been scarce. Iida et al. [6] successfully measured the bubble size distribution and proposed an empirical model [1] to

explain the results. The empirical model was based on the processes of bubble coalescence in the presence of acoustic pressure and bubble dissolution when no acoustic pressure is applied.

We propose to add the process of rectified diffusion (the exchange of gas between bubble and surrounding liquid during bubble oscillations), to add a spatial dimension where bubble movement is governed by the primary Bjerknes force and buoyancy, and include the secondary Bjerknes force in the probability of bubble coalescence.

2. MODEL

A model of bubble oscillations must be employed to calculate the rate of rectified diffusion and Bjerknes force acting on a bubble.

One of the models describing oscillations of bubble volume is the Keller – Miksis equation [3 p.3]:

$$\begin{aligned} \left(1 - \frac{\dot{R}}{c}\right) R \ddot{R} + \frac{3}{2} \dot{R}^2 \left(1 - \frac{\dot{R}}{3c}\right) \\ = \left(1 + \frac{\dot{R}}{c}\right) \frac{p_l}{\rho_l} + \frac{R}{\rho_l c} \frac{dp_l}{dt}, \end{aligned} \quad (2)$$

$$p_l = P_g - p_\infty - \frac{2\sigma}{R} - \frac{4\mu}{R} \dot{R} - p_a(t),$$

where $\dot{R} = \frac{dR}{dt}$, t – time, c – speed of sound, p_l – pressure in the liquid near the bubble, ρ_l – liquid density, P_g – gas pressure, p_∞ – ambient pressure, σ – surface tension, μ – viscosity, $p_a(t)$ – acoustic pressure.

If the amount of gas in the bubble is assumed constant, the gas pressure can be calculated as:

$$P_g = \left(p_\infty + \frac{2\sigma}{R_0}\right) \cdot \left(\frac{R_0}{R}\right)^{3\kappa}, \quad (3)$$

where κ – polytropic coefficient.

Usually, during the acoustic period bubbles subsequently expand and collapse. When the bubble is expanded the gas concentration inside the bubble is lower than the gas concentration in the liquid, and gas flows into the bubble. When the bubble collapses, the gas concentration inside the bubble is higher and gas flows out of the bubble. The net gas exchange is called rectified diffusion.

To calculate the effects of rectified diffusion we use the approach of Meidani [7]. In brief, simultaneously to the bubble oscillations the amount of gas in the bubble is calculated, using the ideal gas model and equations for gas density and temperature, assuming uniform gas density and temperature in the bubble. The convection - diffusion equations are solved for temperature and gas concentration in the liquid. Boundary conditions for the bubble wall come from Henry's law and energy conservation. The equations can be reduced to a system of ordinary differential equations and corresponding numerical methods can be applied. For brevity the model will not be further discussed here, for details refer to [7].

If no acoustic pressure is applied, gas flows out of the bubble because of surface tension. This process is called bubble

dissolution. Analytical treatment of the equilibrium bubble radius change due to dissolution can be found in [8 p.383]:

$$\dot{R}_0 = \frac{C_i D}{\rho_g} \left(\frac{C_{sat}}{C_i} - 1 - \frac{2\sigma}{p_\infty R_0} \right) \left(\frac{1}{R_0} + \frac{1}{\sqrt{\pi D t}} \right), \quad (4)$$

where C_i – gas concentration in the liquid, D – gas diffusion coefficient in the liquid, ρ_g – gas density, C_{sat} – gas saturation concentration. The term containing $\frac{1}{\sqrt{t}}$ is a transient term and therefore it is omitted in calculations of subsequent bubble size distribution.

An approximate analytical treatment of rectified diffusion, describing change in equilibrium bubble radius, using numerically obtained time averages of the bubble radius and its fourth power as well as gas pressure can be found in [8 p.397]:

$$\begin{aligned} \dot{R}_0 = \frac{D R_g T_g C_i}{p_\infty R_0 \left(1 + \frac{4\sigma}{3p_\infty R_0}\right)} \left(\left\langle \frac{R}{R_0} \right\rangle + R_0 \sqrt{\frac{\langle R^4 \rangle}{R_0^4}} \sqrt{\frac{C_{sat}}{\pi D t}} \right) \left(\frac{C_{sat}}{C_i} \right. \\ \left. - \frac{\langle R^4 \rangle \frac{P_g}{p_\infty}}{R_0^4} \right), \end{aligned} \quad (5)$$

where R_g – universal gas constant, T_g – gas temperature.

It can be shown that if a bubble with volume V is located in a pressure field with the pressure gradient ∇p , the force acting on the bubble can be calculated as [8 p.342]:

$$\vec{F} = -V \cdot \nabla p. \quad (6)$$

If the pressure field is the applied acoustic field, the force is called primary Bjerknes force. We assume travelling wave conditions. If the pressure field is created by another bubble, the force is called secondary Bjerknes force and can be calculated as [9]:

$$F_{12} = V_2 \frac{\rho_L}{d^2} \frac{d}{dt} (R_1^2 \dot{R}_1), \quad (7)$$

where F_{12} – is the force that acts on the bubble with volume V_2 and the pressure field is created by the bubble with radius R_1 , d is the distance between bubbles. Bubbles can attract or repel depending on their oscillations, typically bubbles with similar equilibrium radii attract.

The force associated with the inertial properties of bubble is the added mass force F_M [10]:

$$F_M = \frac{1}{2} \rho_L \cdot V \cdot \frac{dv}{dt}, \quad (8)$$

where v is the bubble velocity.

One of the possible descriptions of drag force acting on a moving bubble can be found in [10]:

$$\vec{F}_D = -(\beta_1 \langle R(t) \rangle_{t_0} + \beta_2 \langle R(t) \rangle_{t_0}^2 \cdot |v_{FB1}|) \cdot \vec{v}_{FB1}, \quad (9)$$

where $\langle R(t) \rangle_{t_0}$ is the time-averaged value of the bubble radius, v_{FB1} is the bubble velocity due to the primary Bjerknes force, and $\beta_1 = 0.015 \frac{Ns}{m^2}$, $\beta_2 = 4000 \frac{Ns^2}{m^3}$ are experimentally

determined coefficients [10]. Using the condition for terminal velocity $|\vec{F}_D| = |\vec{F}_{B1}|$, one can easily show that:

$$v_{FB1} = \frac{-\beta_1 + \sqrt{\beta_1^2 + 4 \cdot F_{B1} \cdot \beta_2}}{2 \cdot \beta_2 \langle R(t) \rangle_{t_0}}. \quad (10)$$

For the description of the bubble buoyant terminal velocity v_b , the experimental parameterisation by Patro [11] is used,

$$v_b = a_1 \cdot \frac{1}{3} \cdot g \cdot R^{a_2} \cdot \nu^{a_3}, \quad (11)$$

where g – acceleration due to gravity, ν – viscosity, a_1, a_2, a_3 – experimentally determined coefficients that depend on the bubble radius.

R, μm	a_1	a_2	a_3
<60	0.666	2.00	-1.00
60-150	0.139	1.372	-0.64

To calculate the concentration of bubbles that coalesce N_c^i an approach different from Iida is used. The basic idea is that the number of coalescing bubbles is determined by coalescence probability and bubble concentration:

$$N_c^i = S^i \cdot N_b^i. \quad (12)$$

Similarly to Iida model, only the coalescence of bubbles of equal size is taken into account. Although such an approximation is motivated by computational restrictions, it can be justified by the fact that bubbles with equal radius have the greatest attraction force.

With the use of classical mechanics it can be shown that assuming that only a period-averaged added mass force and the secondary Bjerknes force (with the part independent of spatial coordinate being period averaged) act on a bubble, the time necessary for bubble collision t_{col} can be described as:

$$t_{col} \sim \frac{\sqrt{dd}}{\sqrt{k}}, \quad (13)$$

where

$$k = \frac{\langle 2R(2\dot{R}^2 + R\ddot{R}) \cdot V \rangle_{t_0}}{\langle V \rangle_{t_0}}. \quad (14)$$

We assume that the collision probability S is inverse to the collision time

$$S \sim \frac{1}{t_{col}} \sim \frac{\sqrt{k}}{\sqrt{dd}}. \quad (15)$$

Assuming that bubbles are equally distributed one can approximate that the distance between bubbles d is related with the bubble concentration N_b as:

$$d = N_b^{-\frac{1}{3}}. \quad (16)$$

Therefore we propose to calculate the bubble coalescence probability as:

$$S = h \cdot \sqrt{k} \cdot \sqrt{N_b}, \quad (17)$$

where h is an arbitrary calibration parameter.

The parameters corresponding to the experiments by Iida et al. are used – the acoustic field frequency is 443 kHz, the ultrasound is pulsed, it is turned on for 10'000 acoustic periods and off for 20'000 acoustic periods and each pulse consists of a subsequent ON and OFF period, and results correspond to the

state at the end of the OFF period. It is assumed that when ultrasound is turned on, the processes of bubble generation, coalescence and rectified diffusion are at work, and bubbles move due to the primary Bjerknes force and buoyancy. When the ultrasound is turned off, only dissolution and the buoyancy force affects the bubbles.

The liquid is water, and the gas concentration in the liquid is assumed to be 99% of the saturation gas concentration. The spatial domain is 10 cm long and values used for comparison with experimental results correspond to $z=7.5$ cm according to the description of the experimental setup.

There are interesting results concerning bubble generation in the crevices [12], however the applicability is limited because usually the properties of an arbitrary surface in the experimental setup are not known and we assume homogeneous bubble nucleation.

At the beginning of the pulse the bubbles are generated, using the flat generation rate approach by Iida. For every interval of bubble radius, smaller than R^{cut} constant bubble volume is generated. The total generation volume V_{gen} and R^{cut} are parameters to be calibrated.

The interval of bubble radii used in calculations is $10^{-6.3}$ to $10^{-3.3}$ m divided into 155 logarithmically spaced intervals. The spatial dimension is divided into 400 equally spaced intervals. The precision was tested and no significant changes were observed when the number of intervals was increased twofold and the time step was halved.

The number of bubbles changing their radius n_R^i during the time step Δt , can be calculated as:

$$\frac{n_R^i}{n_b^i} = \frac{\frac{dR}{dt}(R^i) \cdot \Delta t}{\Delta R^i}, \quad (18)$$

where the number of bubbles in the i -th interval is n_b^i , the bubble interval has size ΔR^i and the average bubble radius in the interval is R^i .

Similarly, the number of bubbles changing their spatial position n_z^i if their velocity due to the force F is v_F^i can be calculated as:

$$\frac{n_z^i}{n_b^i} = \frac{v_F^i \cdot \Delta t}{\Delta z}, \quad (19)$$

where Δz is the length of the spatial interval.

It is assumed that the ultrasonic transducer is placed at the bottom of the spatial domain and at the top is the free liquid surface, where bubbles if they move upwards leave the system joining with the air. Bubbles that are smaller than the smallest calculated radius interval are considered dissolved. The number of bubbles growing larger than the chosen calculation range of radius is insignificantly small.

The model system is programmed in Matlab (calculations of bubble oscillations and rectified diffusion) and in Delphi (the bubble size distribution model). The computational time needed for calculations of bubble oscillations exceeded time needed for bubble size distribution calculations, because of the fine grid needed for the liquid domain to ensure accuracy of rectified diffusion values.

2. RESULTS

The model of rectified diffusion can be used to numerically calculate bubble dissolution, simply assuming zero acoustic pressure. The numerical results of bubble dissolution show good agreement with theoretical predictions (Fig. 1). Therefore, in subsequent bubble size distributions, the analytically obtained values of the bubble dissolution rate will be used.

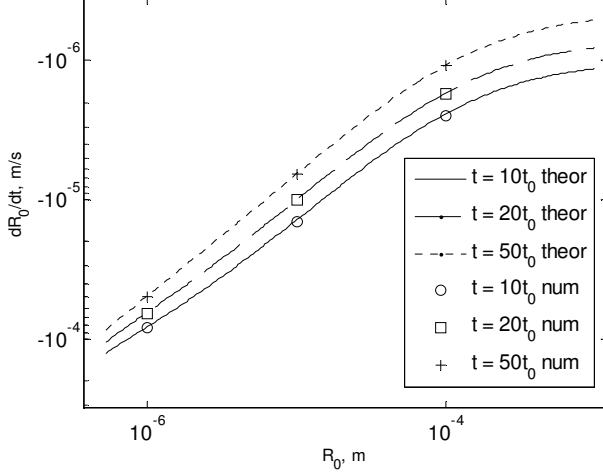


Fig. 1. Comparison of theoretical and numerical dissolution values.

There exists a significant problem considering the numerical results of rectified diffusion. Theoretical and simulation results agree that there exists a transition period before the value of rectified diffusion converges to a constant. Therefore calculations of bubble oscillations of 400 acoustic periods for bubbles much smaller than the resonance radius and of 1000 periods for bubbles much larger than the resonance radius were performed before the calculation of the average values of rectified diffusion for each equilibrium radius. However, the change in bubble radius for bubbles near the resonance size is so rapid that it is unclear whether the value of rectified diffusion after, for example, one hundred acoustic periods can be ascribed to the initial bubble radius, because of the fact that the rate of rectified diffusion depends on bubble oscillations that depend on the equilibrium bubble radius must be taken into account. To circumvent this problem, for bubble sizes near the resonance radius (2-6 μm) the value of rectified diffusion was calculated, first, by calculating the growth of five bubbles with different initial radius through the region and recording the values of equilibrium bubble radius and rectified diffusion at every acoustic period and then averaging and smoothing the data.

A comparison of the numerically obtained results with analytical predictions obtained using equations (2), (3) and (5) is shown in Fig. 2. In order to depict both negative and positive values of rectified diffusion in one figure in double-logarithmic axes the absolute value is plotted on the y axis and the colour represents the sign. It can be seen that the theoretical and numerical results agree for bubbles much smaller and much larger than the resonance radius, however, for bubbles near the resonance radius the numerical values are much larger than the

ones obtained theoretically. Therefore, in subsequent calculations the numerically obtained values will be used.

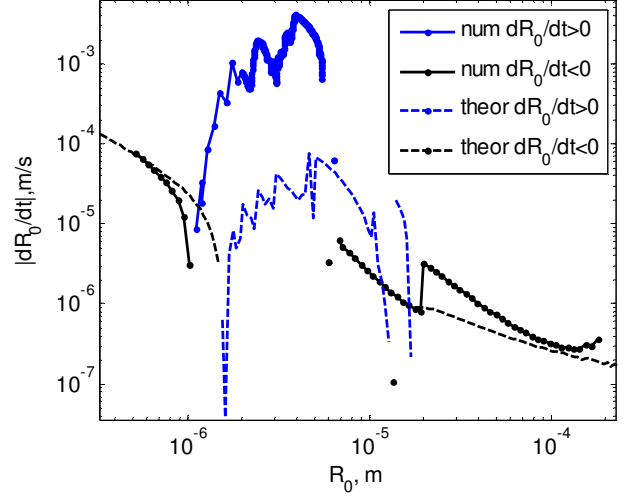


Fig. 2. Rectified diffusion as a function of initial bubble radius. Comparison of numerical results and values obtained from (2), (3) and (5) ($t = 1000t_0$).

An interesting phenomenon was observed during the calculations of rectified diffusion – when the value of rectified diffusion became negative, the bubble initially shrank, but subsequently changed the oscillation mode and continued to grow, marking a loop-like trajectory in the phase space, see. Fig. 3.

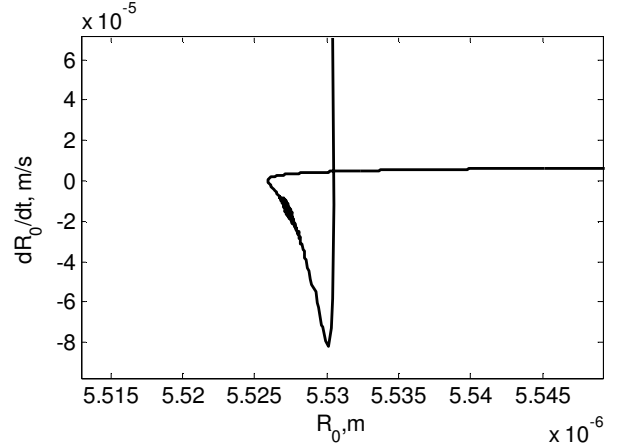


Fig. 3. Fragment of the bubble trajectory in the phase space. Calculations started with $R_0 = 2 \mu\text{m}$.

The values of primary and secondary Bjerknes force were calculated using the bubble oscillation data. The dimensionless coefficient \bar{k}_V

$$\bar{k}_V = k_V \cdot \frac{t_0^2}{R_0^3}$$

representing the contribution input of the secondary Bjerknes force in coalescence coefficient is plotted in

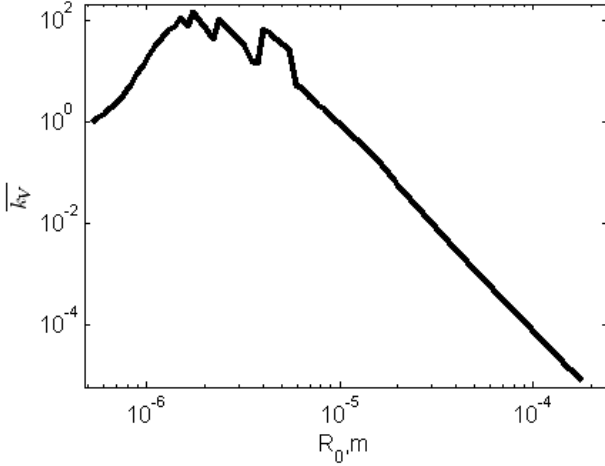


Fig. 4. As expected, it has positive value (representing attraction between bubbles) for all bubble sizes considered. Results show that the largest attraction force exists between bubbles near the resonance radius, large and small bubbles have a considerably smaller attraction force for equally sized bubbles.

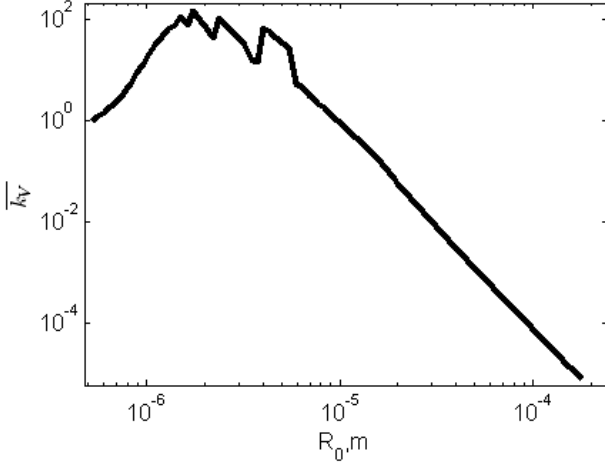


Fig. 4. Dimensionless coefficient $\overline{k_V}$ representing the influence of secondary Bjerknes force in the coalescence coefficient as a function of initial bubble radius.

The primary Bjerknes force is proportional to the initial bubble radius (Fig. 5) with some local maxima that are related to the violent bubble oscillations near the resonant bubble radius.

The bubble terminal velocities due to the primary Bjerknes force and due to gravity as a function of the equilibrium bubble radius are shown on Fig. 6. It can be seen that the bubble terminal velocity due to the primary Bjerknes force is considerably larger than that due to gravity. Local maxima in the values of terminal velocity correspond to local maxima in the values of primary Bjerknes force (Fig. 5).

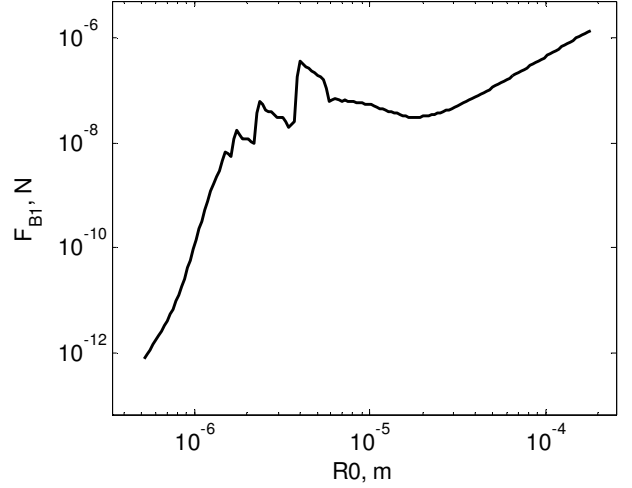


Fig. 5. Primary Bjerknes force as a function of initial bubble radius.

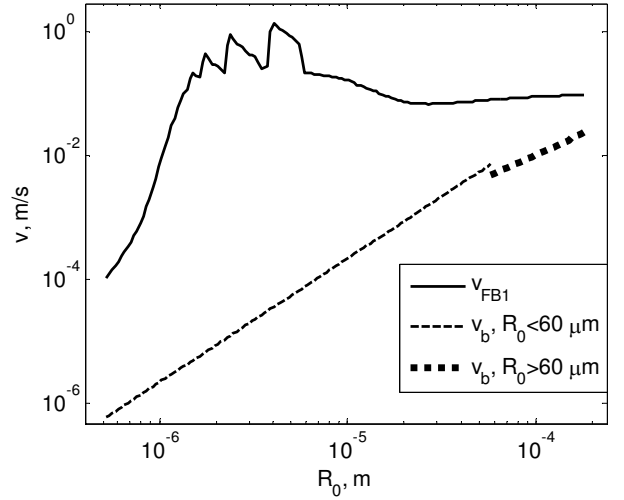


Fig. 6. Bubble terminal velocities for bubble movement due to the primary Bjerknes force and buoyancy force.

The processes of dissolution (Fig. 1), rectified diffusion (Fig. 2), coalescence (Fig. 4) and spatial movement due to primary Bjerknes force and buoyancy (Fig. 6) are used to calculate the bubble size distribution in space and time. The calculations showed that good agreement with experiment can be obtained for the average bubble radius (Fig. 7) and the total bubble volume (Fig. 8) if the $V_{gen} = 15.0 \text{ nL/cm}^3$ and $R^{cut} = 2 \mu\text{m}$, and the coalescence coefficient $h = 2.5$. The average bubble radius for a bubble size distribution is defined as a bubble radius, where half of the total volume of the bubbles is contained in bubbles that have a radius smaller than the average bubble radius. The effect causing the ladder like structure in Fig. 7 is a numerical one – values of the average bubble radius are placed in the middle of the corresponding bubble size interval. The experimental and numerical results agree that after a number of pulses, a steady state, where the average bubble radius does not change, is reached. However, the numerical results predict the

onset of a steady state much later and at much larger radii than the experimental results.

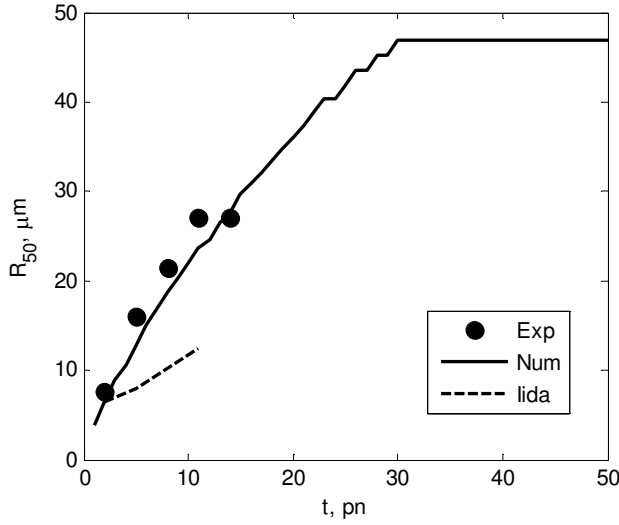


Fig. 7. Average bubble radius as a function of pulse number. Comparison between numerical results and experimental and numerical results acquired by Iida [6],[1].

The model replicates the linear increase in bubble volume (Fig. 8), and the onset of steady state can be observed at the same time when the average bubble radius reaches constant value.

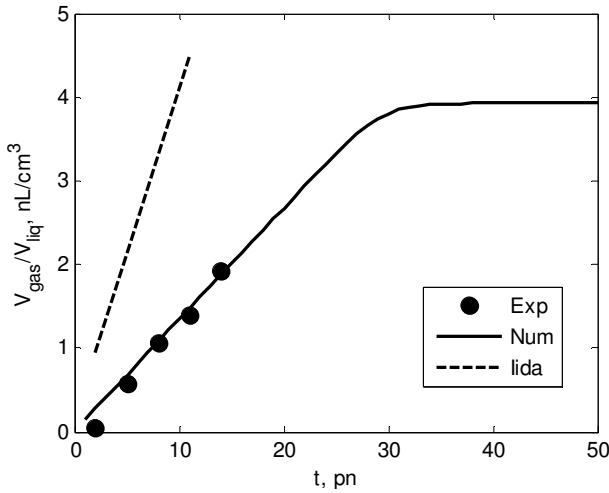


Fig. 8. Bubble volume as a function of pulse number. Comparison between numerical results and experimental and numerical results acquired by Iida [6],[1].

From the distribution of bubble volume over the radius (Fig. 9) it can be concluded that the model predicts that the volume of gas contained in smaller bubbles reaches a constant value sooner. Several hypothesis regarding discrepancies between experiments and simulations can be proposed. First, it is possible that the current model of coalescence overestimates the coalescence rate of large bubbles; second, the bubble fragmentation could be responsible for reducing the number of large bubbles and should be included in the model.

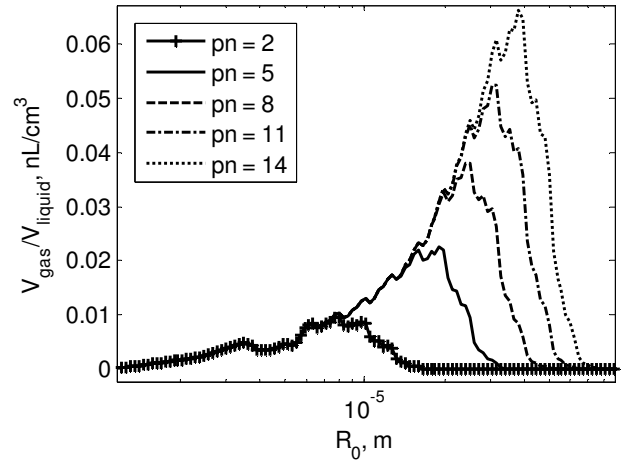


Fig. 9. The bubble volume distribution as a function of size for different pulse numbers. Numerical results.

The integral amount of gas transported between bubbles, the liquid and the water surface during the on and off periods of the ultrasound pulse is compared in Fig. 10. Results show that the most important process is the bubble dissolution followed by bubble transport due to the primary Bjerknes force. Rectified diffusion has a considerably smaller influence. The amount of gas exchanged because of dissolution remains constant over time because dissolution mainly affects the smaller bubbles and the volume of smaller bubbles remains unchanged (Fig. 9). The increase of the number of larger bubbles results in an increased volume of gas that leaves the system through the water surface, because the terminal velocity for larger bubbles is roughly constant but larger bubbles have greater volume.

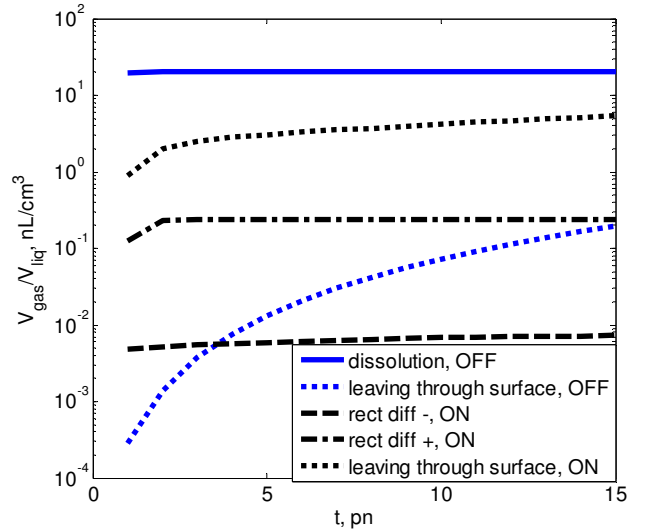


Fig. 10. Integral values of the gas transport between bubbles, liquid and water surface as a function of pulse number. Dissolution and leaving through the surface are shown when the acoustic field is switched off.

The data concerning bubble spatial distribution (Fig. 11) show that at the beginning the distribution is homogenous but at later times there are significantly more bubbles near the top of the liquid. A similar trend can be observed in experimental results by Lee [13].

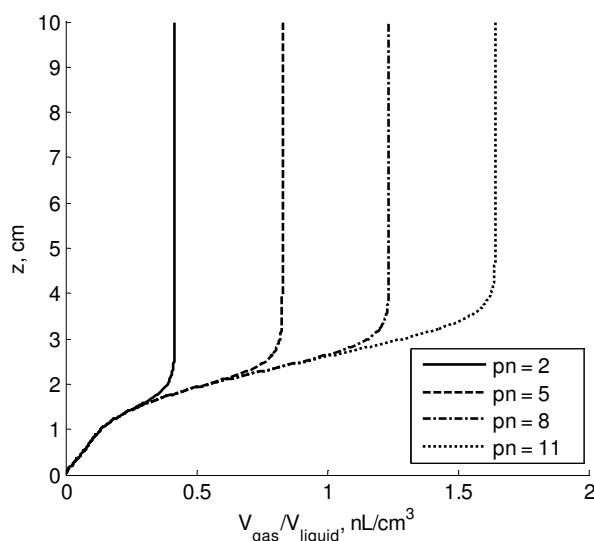


Fig. 11. Spatial distribution of bubbles for different pulse numbers.

4. CONCLUSIONS.

An improved bubble size distribution model was successfully implemented. Results show perfect agreement between theoretical and analytical dissolution values; however the analytical approach underestimates the value of rectified diffusion when compared to the numerical solution. Using calibration of unknown parameters model results can be fitted to experimental results, however the model predicts much larger steady state average bubble radius and it is reached at later times than the experiments suggest. In order to improve the model, a theoretical treatment for bubble generation and coalescence would be preferable and coalescence of bubbles with different sizes should be included. Bubble fragmentation should be taken into account in case it could explain the lesser amount of larger bubbles seen in the experiments in contrast to the model. In order to explain the spatial bubble distribution better the absorption of the ultrasound in the bubbles should be taken into account.

ACKNOWLEDGMENTS

The work has been carried out at the University of Latvia and the financial support by European Social Fund (ESF), project contract No.

2009/0223/1DP/1.1.1.2.0/09/APIA/VIAA/008 and

2009/1062/1DP/1.1.2.1.1/09/IPIA/VIAA/004

is gratefully acknowledged.

REFERENCES

1. Iida, Y, et al. Bubble population phenomena in sonochemical reactor: II. Estimation of bubble size distribution and its number

density by simple coalescence model calculation. *Ultrasonics Sonochemistry*. 2010, Vol. 17, p. 480-486.

2. Kim, W, et al. Mechanism of particle removal by megasonic waves. *Applied Physics Letters*. 2009, Vol. 24, p. 081908.

3. Lauterborn, W and Thomas, K. Physics of bubble oscillations. *Reports on Progress in Physics*. 2010, Vol. 73, p. 6501.

4. Mettin, R and Doinikov, A A. Translational instability of a spherical bubble in a standing ultrasound wave. *Applied Acoustics*. 2009, Vol. 70, p. 1330-1339.

5. Doinikov, A A. Translational motion of two interacting bubbles in a strong acoustic field. *Physical Review E*. 2001, Vol. 64, p. 026301.

6. Iida, Y, et al. Bubble population phenomena in sonochemical reactor: I Estimation of bubble. *Ultrasonics Sonochemistry*. 2010, Vol. 17, p. 473-479.

7. Meidani, A. R. N. and Hasan, M. Mathematical and physical modelling of bubble growth due to ultrasound. *Applied Mathematical Modelling*. 2004, Vol. 28, 4, p. 333-351.

8. Leighton, T G. *The Acoustic Bubble*. London : Academic Press, 1994.

9. Mettin, R, et al. Bjerknes forces between small cavitation bubbles in a strong acoustic field. *Physical Review E*. 1997, Vol. 56, 3, p. 2924-2931.

10. Parlitz, U, et al. Spatio-temporal dynamics of acoustic cavitation bubble clouds. *Phil. Trans. R. Soc. Lond. A*. 1999, Vol. 357, p. 313-334.

11. Patro, R, Leifer, I and Bowyer, P. Better bubble process modeling: Improved bubble hydrodynamics parameterization. [book auth.] M Donelan. *Gas Transfer and Water Surfaces*. Washington, D.C.: AGU, 2002.

12. Borkent, B M, et al. Nucleation threshold and deactivation mechanisms of nanoscopic cavitation nuclei. *Physics of Fluids*. 2009, Vol. 21, p. 102003.

13. Lee, J, et al. Development and optimization of acoustic bubble structures at high frequencies. *Ultrasonics Sonochemistry*. 2011, Vol. 18, 1, p. 92-98.

On surface cleaning by laser-induced cavitation bubbles

Fabian Reuter, Karsten Köhler, Robert Mettin

*Georg-August-Universität Göttingen,
Drittes Physikalisches Institut, CD-Laboratory for Cavitation and Micro-Erosion,
Friedrich-Hund-Platz 1, 37077 Göttingen, Germany*

The dynamics and erosive action of bubbles collapsing close to solid surfaces is a well-known and frequently investigated phenomenon. Nevertheless, open questions remain, in particular about the detailed events taking place at the final stages of collapse. Here, we investigate the removal of attached particles (cleaning) from flat or structured solid surfaces by pulse laser-induced bubbles. Investigations are conducted by means of highspeed videography, particle image velocimetry (PIV), and acoustical measurements. The main parameter for the control of bubble collapse dynamics as well as particle removal is the normalised stand-off $\gamma = d / R_{max}$ with the bubble centre distance d from the surface, and the maximum bubble radius R_{max} . It appears that several distinct mechanisms can be responsible for the particle detachment, including shockwave emission, ring vortex shedding, and jet impact. Which mechanism prevails seems to depend on the stand-off, but also on the type of attached particles. Furthermore, non-flat wall geometries are investigated in experiment and numerical simulations.